Simplified Virtual Synchronous Compensator with Grid–Forming Capability

Original
Simplified Virtual Synchronous Compensator with Grid–Forming Capability / Mallemaci, V., Mandrile, F., Carpaneto, E., Bojoi, R.. - In: IEEE TRANSACTIONS ON INDUSTRY APPLICATIONS. - ISSN 0093-9994. - ELETTRONICO. - (2023), pp. 1-17. [10.1109/TIA.2023.3285523]

Publisher:
IEEE

Published
DOI:10.1109/TIA.2023.3285523

This article has been accepted for publication in IEEE Transactions on Industry Applications. This is the author's version which has not been fully edited and content may change prior to final publication. Citation information: DOI 10.1109/TIA.2023.3285523

Simplified Virtual Synchronous Compensator with Grid–Forming Capability

Vincenzo Mallemaci, *Student Member, IEEE*, Fabio Mandrile, *Member, IEEE*,
Enrico Carpaneto, *Member, IEEE*, and Radu Bojoi, *Fellow, IEEE*

***Abstract*—The Simplified Virtual Synchronous Compensator (S–VSC) is a Virtual Synchronous Machine (VSM) solution available in the literature, which operates as a virtual compensator. Previous works demonstrated that it can provide grid services (e.g., inertial behavior, grid support during faults) only in grid–following operation. However, the grid–forming capability of the S–VSC (and in general of a virtual compensator) has never been investigated in the literature. Therefore, this paper proposes an S–VSC model able to operate both in grid–following and in grid–forming configuration. First, the paper validates the small–signal stability of the control algorithm both in grid–mode and island operation through an eigenvalue–based stability analysis. Next, the control algorithm is experimentally validated on a 15 kVA inverter connected to a scaled microgrid. The experimental tests demonstrate that the S–VSC can operate both as grid–following and grid–forming. Moreover, it can seamlessly switch from the grid–connected to the island operation without requiring any communication system. Finally, the grid–forming capability of the S–VSC is experimentally validated even in case of a fault occurrence, thus representing a valid solution for the control of a microgrid.**

***Index Terms*—Grid–forming, Microgrid, Virtual Synchronous Compensator, Virtual Synchronous Machine**

I. INTRODUCTION

THE the power system is currently experiencing a transition from the centralized to the distributed energy production, especially from renewable energy sources (RESs). In this context, the spread of microgrids (MGs) represents a valid solution to integrate more efficiently the distributed energy resources [1]–[3]. However, a predominance of inverter–interfaced power plants would reduce the total inertia of the power system, compromising its frequency and voltage stability. To limit these issues, renewable energy power plants are required to provide grid services (e.g., inertial behavior, harmonic compensation), grid support, as well as operation in island–mode [4], [5], as performed by conventional synchronous machines (SMs) [6]. Unfortunately, the provision of such services cannot be guaranteed by the standard control techniques for RESs, e.g., Maximum Power Point Tracking (MPPT). To overcome this limitation, a promising solution is to make grid–connected inverters able to behave as conventional SMs, by applying the concept of Virtual Synchronous Machine (VSM). Many different VSM models have been proposed in the last years [7]–[19]. A particular solution available in the literature is the Simplified Virtual Synchronous Compensator (S–VSC) model [20], which operates as a synchronous compensator, so it is in charge only of the provision of the grid services, leaving the power generation to the classical inverter structure. This is the main peculiarity and advantage of the S–VSC compared to other VSM solutions available in the literature. Indeed, the S–VSC generates additive power contributions to the inverter references, to provide grid services. Instead, in the literature, VSMs are typically in charge of processing the full power. Therefore, the S–VSC always operates at low load, featuring better transient stability and damping [9], [20]. Previous papers demonstrated that the S–VSC model can provide inertial behavior, grid support during faults and harmonic compensation in grid–following operation [20], [21]. However, it has never been examined whether the S–VSC can operate even in island–mode. Therefore, this paper proposes a solution for the control of a microgrid both in grid–connected and island–mode, based on the S–VSC control algorithm. The proposed S–VSC model is able to provide all the aforementioned grid services, including the island capability, in a microgrid whose block scheme is

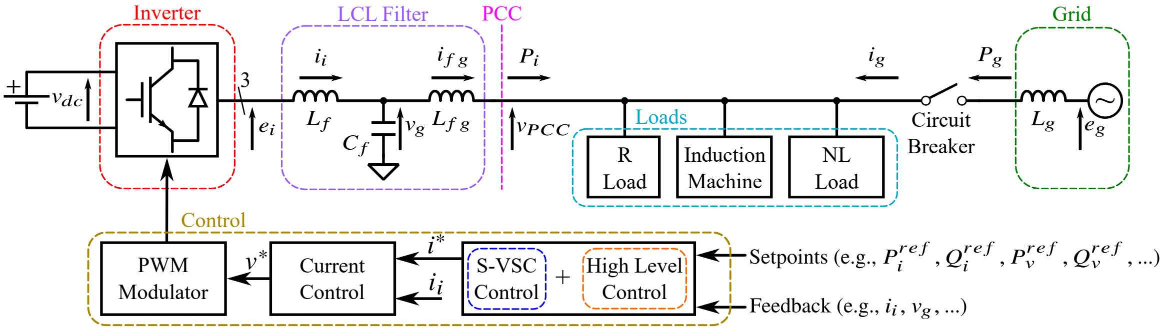

Fig. 1. Block scheme of the microgrid under study.

V. Mallemaci, F. Mandrile, E. Carpaneto and R. Bojoi are with the Dipartimento Energia "G. Ferraris", Politecnico di Torino, Torino, 10129, Italy (e-mail: vincenzo.mallemaci@polito.it)

This article has been accepted for publication in IEEE Transactions on Industry Applications. This is the author's version which has not been fully edited and content may change prior to final publication. Citation information: DOI 10.1109/TIA.2023.3285523

depicted in Fig. 1. The system consists of a three phase inverter connected to the grid through an LCL filter. Moreover, three loads are connected at the point of common coupling (PCC): a resistive load (R load), an induction machine (IM) and a non–linear load (NL load). Finally, a circuit breaker is located between the PCC and the grid. If the circuit breaker is opened, the microgrid is isolated from the rest of the power system. The inverter is supplied by an ideal dc–source (representing, e.g., a storage system) and it is controlled according to the S–VSC control algorithm.

The main paper contribution is the extension of the S–VSC model both in grid–connected (i.e., grid–following operation) and island–mode (i.e., grid–forming operation). First, the small–signal stability of the control has been validated through an eigenvalue–based analysis. Next, experimental tests demonstrated that the S–VSC can operate both in grid–following and grid–forming configurations. Secondly, this paper shows that the S–VSC can seamlessly switch from the grid–connected to the island operation in case of a sudden opening of the circuit breaker (Fig. 1) without any feedback of the grid connection. Finally, experimental tests demonstrate that the S–VSC can operate in island–mode even in case of a fault occurrence. During the fault, the current is saturated. As soon as the fault is cleared, the system returns to the normal operating condition.

This paper is an extension of [22], where the grid–forming capability of the S–VSC was preliminary validated. In particular, the following additions have been performed:

- A section describing the state–space modeling of the system under study has been included;
- An eigenvalue–based analysis and a modal analysis have been performed to validate the small–signal stability of the control both in grid–mode and island operation;
- The difference between the existing S–VSC model and the proposed S–VSC is highlighted through an experimental test;
- The grid–forming capability of the S–VSC is experimentally tested even in case of a fault occurrence.

This paper is divided as follows. Section II describes the original structure of the S–VSC model together with the scaled microgrid under study. In Section III the complete version of the S–VSC model with grid–forming capability is presented. The state–space model of the system is proposed in Section IV both for the grid–connected and the island configuration. Section V provides the small–signal stability analysis of the control in both operating conditions. The experimental validation of the control is proposed in Section VI. Finally, the conclusions of the paper are provided in Section VII.

II. S–VSC MODEL

The S–VSC is a voltage–input, current–output virtual synchronous machine. The block scheme is illustrated in Fig. 2. All the quantities are in per unit (pu), referred to the base values listed in Table I. The S–VSC model consists of the following main blocks:

- *Electrical Equations*: it implements the S–VSC virtual stator equations in the (d, q) reference frame rotating at the virtual rotor speed ω_r. The inputs of the block are the measured capacitor voltage v_g, the virtual rotor position θ_r, the virtual rotor speed ω_r and the virtual excitation flux λ_e. The output is the virtual current i_v. The equations in the (d, q) reference frame are the following:

$$v_{gd} = -R_v i_{vd} - \omega_r \lambda_q + \frac{1}{\omega_b}\frac{d\lambda_d}{dt} \tag{1}$$

$$v_{gq} = -R_v i_{vq} + \omega_r \lambda_d + \frac{1}{\omega_b}\frac{d\lambda_q}{dt} \tag{2}$$

$$\frac{L_{rq}}{\omega_b R_{rq}}\frac{d\lambda_{rq}}{dt} = -\lambda_{rq} - L_{rq} i_{vq} \tag{3}$$

$$i_{vd} = \frac{\lambda_e - \lambda_d}{L_d^{''}} \tag{4}$$

$$i_{vq} = \frac{\lambda_{rq} - \lambda_q}{L_q^{''}} \tag{5}$$

where R_v is the virtual resistance, λ_d and λ_q are the d, q components of the virtual stator flux linkages, $L_d^{''}$ and $L_q^{''}$ are the machine subtransient inductances, equal to the virtual inductance L_v (i.e., subtransient isotropic machine), λ_{rq} is the damper winding flux linkage and R_{rq}, L_{rq} are the parameters of the q–axis virtual damper winding [20].
- *Mechanical Emulation*: this blocks embeds the swing equation of the virtual synchronous machine [6], i.e., the relationship which describes the mechanical behavior of the S–VSC model. It provides both ω_r and θ_r from the virtual active power P_v and the virtual active power reference P_v^*. The swing equation is:

$$P_v^* - P_v = 2H\frac{d\omega_r}{dt} \tag{6}$$

where H is the inertia constant (s);
- *Excitation Control*: it receives as inputs the virtual reactive power Q_v and the virtual reactive power reference Q_v^* to regulate the excitation flux λ_e and the reactive power exchange with the grid [23], according to (7):

$$\lambda_e = \int k_e \frac{Q_v^* - Q_v}{V_g} dt \tag{7}$$

$$k_e = \frac{L_v + L_{fg} + L_g}{\tau_e} \tag{8}$$

where k_e is the excitation gain in per unit and τ_e is the excitation time constant (s).

The S–VSC can autonomously synchronize to the grid with no need of additional algorithms, e.g., phase locked loop (PLL) [20]. The virtual power references P_v^* and Q_v^* are equal to the external virtual references P_v^{ref} and Q_v^{ref}. As the S–VSC works as a virtual compensator in normal operating conditions, then they are always set to zero. The inverter power references P_i^* and Q_i^* are respectively equal to the external active power reference P_i^{ref} and the external reactive power reference Q_i^{ref}. P_i^{ref} and Q_i^{ref} come from an external control law (e.g., MPPT, dc–link voltage control for a non–ideal dc–source). The current reference i_i^* is retrieved from the Power to Current block. Next, the virtual current i_v is added to the reference i_i^* to provide the ancillary services. Both the VSM and the inverter control parameters are tuned according to [20].

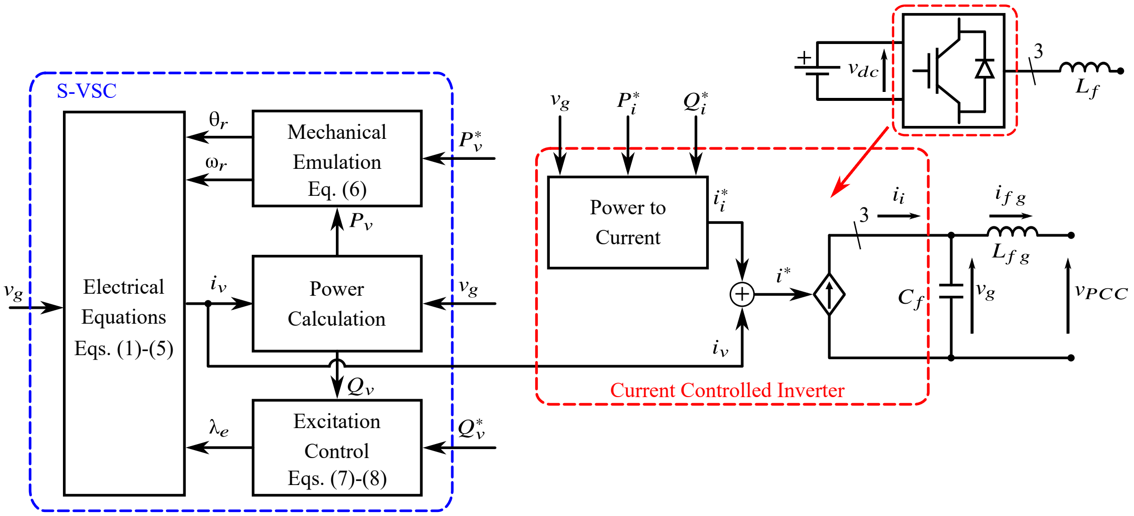

Fig. 2. Block scheme of the inverter controlled according to the S–VSC model.

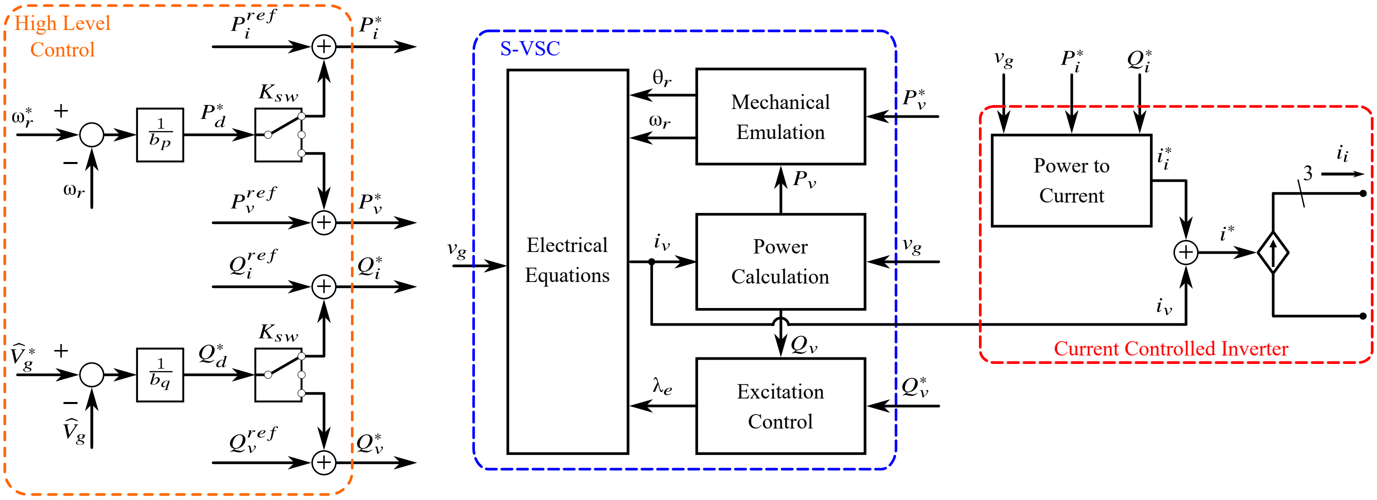

Fig. 3. Block scheme of the inverter controlled according to the S–VSC model with the High Level control.

III. HIGH LEVEL CONTROL

The grid–forming capability of the S–VSC model is obtained by adding the High Level control block illustrated in Fig. 3 to the original structure of Fig. 2.

The High Level control consists of two external control loops. The first control loop is the active droop control law, responsible for the proportional regulation of the frequency, during both grid–connected and island operation:

$$P_d^* = \frac{\omega_r^* - \omega_r}{b_p} \tag{9}$$

where P_d^* is the active power droop reference, ω_r^* is the speed reference and b_p is the active droop coefficient. This is set to the conventional value of 2% [6].

The second external controller is the reactive droop control law, in charge of the proportional regulation of the voltage amplitude $\widehat{V}_g$, both in grid–mode and island operation:

$$Q_d^* = \frac{\widehat{V}_g^* - \widehat{V}_g}{b_q} \tag{10}$$

where Q_d^* is the reactive power droop reference, $\widehat{V}_g^*$ is the voltage reference and b_q is the reactive droop coefficient, set to the conventional value of 50% [6].

These two external loops enable the grid–forming capability of the S–VSC model, while preserving the superior performance of the compensator operation with respect to classical VSMs [20]. Moreover, thanks to the High Level control, the S–VSC can actuate the primary frequency and voltage regulation during the grid–connected operation.

According to the multiport logical switch K_{sw} in Fig. 3, the two references P_d^* and Q_d^* can be:

- added to P_i^{ref} and Q_i^{ref} to retrieve P_i^* and Q_i^*. In this case, $P_v^* = P_v^{ref}$ and $Q_v^* = Q_v^{ref}$;
- not used (i.e., the High Level control is disabled);
- added to P_v^{ref} and Q_v^{ref} to retrieve P_v^* and Q_v^*. In this case, $P_i^* = P_i^{ref}$ and $Q_i^* = Q_i^{ref}$.

In this paper, the references P_d^* and Q_d^* are always added to the inverter external references, thus preserving the compensator operation.

In grid–connected mode, the S–VSC operates as a grid–following converter. Therefore, it injects power into the grid according to the power references P_i^* and Q_i^*. Moreover, it provides all the aforementioned grid services. In island–mode, the S–VSC operates as grid–forming. In this case, it provides the power requested by the loads.

IV. STATE–SPACE MODELING

In this paper, the small–signal stability of the S–VSC control algorithm is evaluated both in grid–mode and island operation by means of an eigenvalue–based stability analysis as in [24], [25]. First, the state–space model of the entire system depicted in Fig. 1 is needed. A widely–adopted solution in the literature is to retrieve the state–space model of each element of the system and then apply the Component Connection Method (CCM) [24]–[26]. This technique consists of merging the state–space models of each subsystem into the overall state–space representation of the entire system in a modular manner. Each k–th subsystem is written in the state–space form of (11):

$$\begin{cases} \dfrac{d\mathbf{x_k}}{dt} = \mathbf{A_k x_k} + \mathbf{B_k u_k} & \\ \mathbf{y_k} = \mathbf{C_k x_k} + \mathbf{D_k u_k} & \end{cases} \qquad k = 1 \dots \mathrm{n} \tag{11}$$

where the vectors $\mathbf{x_k}$, $\mathbf{u_k}$ and $\mathbf{y_k}$ are, respectively, the state variables, the inputs and the outputs of the k–th subsystem. The matrices $\mathbf{A_k}$, $\mathbf{B_k}$, $\mathbf{C_k}$ and $\mathbf{D_k}$ are the subsystem state–space matrices. The total number of the subsystems is n.

Next, the aggregated model is obtained by merging the subsystems matrices as follows:

$$\begin{cases} \dfrac{d\mathbf{x_s}}{dt} = \mathbf{A x_s} + \mathbf{B u} \\ \mathbf{y} = \mathbf{C x_s} + \mathbf{D u} \end{cases} \tag{12}$$

$$\begin{cases} \mathbf{x_s} = [\mathbf{x_1} \dots \mathbf{x_n}]^{\mathrm{T}} \\ \mathbf{u} = [\mathbf{u_1} \dots \mathbf{u_{n+m}}]^{\mathrm{T}} \\ \mathbf{y} = [\mathbf{y_1} \dots \mathbf{y_{n+m}}]^{\mathrm{T}} \end{cases} \tag{13}$$

$$\mathbf{A} = \begin{bmatrix} \mathbf{A_1} & 0 & \cdots & 0 \\ 0 & \mathbf{A_2} & \cdots & 0 \\ \vdots & \vdots & \ddots & \vdots \\ 0 & 0 & \cdots & \mathbf{A_n} \end{bmatrix} \tag{14}$$

$$\mathbf{B} = \begin{bmatrix} \mathbf{B_1} & 0 & \cdots & 0 & \overbrace{0 \quad \cdots \quad 0}^{\text{number of algebraic blocks inputs}} \\ 0 & \mathbf{B_2} & \cdots & 0 & 0 \quad \cdots \quad 0 \\ \vdots & \vdots & \ddots & \vdots & \vdots \quad \ddots \quad \vdots \\ 0 & 0 & \cdots & \mathbf{B_n} & 0 \quad \cdots \quad 0 \end{bmatrix} \tag{15}$$

$$\mathbf{C} = \left[\begin{array}{cccc} \mathbf{C_1} & 0 & \cdots & 0 \\ 0 & \mathbf{C_2} & \cdots & 0 \\ \vdots & \vdots & \ddots & \vdots \\ 0 & 0 & \cdots & \mathbf{C_n} \\ 0 & \cdots & \cdots & 0 \\ \vdots & \vdots & \ddots & \vdots \\ 0 & \cdots & \cdots & 0 \end{array}\right] \begin{array}{l} \\ \\ \\ \\ \left.\begin{array}{l} \\ \\ \\ \end{array}\right\} \text{number of algebraic blocks outputs} \end{array} \tag{16}$$

$$\mathbf{D} = \begin{bmatrix} \mathbf{D_1} & 0 & \cdots & 0 \\ 0 & \mathbf{D_2} & \cdots & 0 \\ \vdots & \vdots & \ddots & \vdots \\ 0 & 0 & \cdots & \mathbf{D_{n+m}} \end{bmatrix} \tag{17}$$

where $\mathbf{x_s}$, $\mathbf{u}$ and $\mathbf{y}$ are, respectively, the aggregated state variables, inputs and outputs of the system; the matrices $\mathbf{A}$, $\mathbf{B}$, $\mathbf{C}$ and $\mathbf{D}$ are the aggregated state–space matrices; m is the number of algebraic blocks [25].

Next, the CCM can be applied. The aggregated matrices are connected through the so–called interconnection matrices $\mathbf{L_{uy}}$, $\mathbf{L_{us}}$, $\mathbf{L_{sy}}$ and $\mathbf{L_{ss}}$, as follows:

$$\begin{cases} \mathbf{u} = \mathbf{L_{uy} y} + \mathbf{L_{us} u_s} \\ \mathbf{y_s} = \mathbf{L_{sy} y} + \mathbf{L_{ss} u_s} \end{cases} \tag{18}$$

where $\mathbf{u_s}$ and $\mathbf{y_s}$ are, respectively, the inputs and the outputs of the overall system, while $\mathbf{x_s}$ is the state variables vector of the system.

Finally, the state–space representation of the entire system is the following:

$$\begin{cases} \dfrac{d\mathbf{x_s}}{dt} = \mathbf{A_s x_s} + \mathbf{B_s u_s} \\ \mathbf{y_s} = \mathbf{C_s x_s} + \mathbf{D_s u_s} \end{cases} \tag{19}$$

where:

$$\begin{cases} \mathbf{A_s} = \mathbf{A} + \mathbf{B L_{uy} W C} \\ \mathbf{B_s} = \mathbf{B L_{uy} W D L_{us} B L_{us}} \\ \mathbf{C_s} = \mathbf{L_{sy} W C} \\ \mathbf{D_s} = \mathbf{L_{sy} W D L_{us}} + \mathbf{L_{ss}} \\ \mathbf{W} = \left(\mathbf{I} - \mathbf{D L_{uy}}\right)^{-1} \end{cases} \tag{20}$$

The subsystems of the system under analysis are: the High Level control, the S–VSC control, the reference calculation (i.e., Power to Current block and current reference calculation), the inverter, the LCL filter, the loads block and the grid. The S–VSC control block consists of two sub–blocks: Electrical Equations and power loops (i.e., Mechanical Emulation and Excitation Control). The inverter block consists of the PI current controller and the control delay [25]. All the state–space models are linearised around an equilibrium point, thus obtaining the small–signal models. The symbol ”Δ” defines the variation of the quantity around the equilibrium point, while the subscript ”0” defines the quantity value at the equilibrium point. Moreover, the models are written in the (d, q) reference frame rotating at the virtual speed ω_r. The grid voltage vector is aligned to the q–axis. All the equations are written in per unit, referred to the base values listed in Table I. The state–space models are proposed in Appendix A, the CCM for the three loads in Appendix B, the CCM for the grid–mode in Appendix C and the CCM for the island configuration in Appendix D.

The state–space models have been validated by means of PLECS simulations and experimental tests. Fig. 4 shows a 0.1 pu IM load step change while the resistive load is connected, the NL load is disconnected and the system operates in grid–connected configuration. A similar test is repeated for the island operation and the result is illustrated in Fig. 5. In this

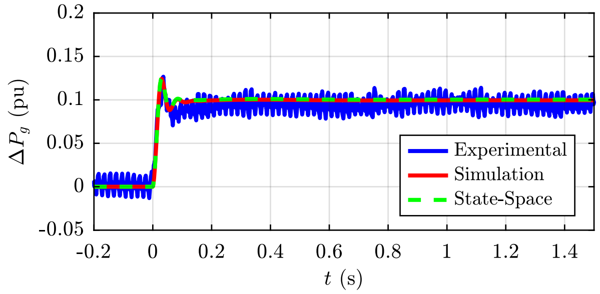

Fig. 4. Grid power variation to an IM load change in grid–connected operation.

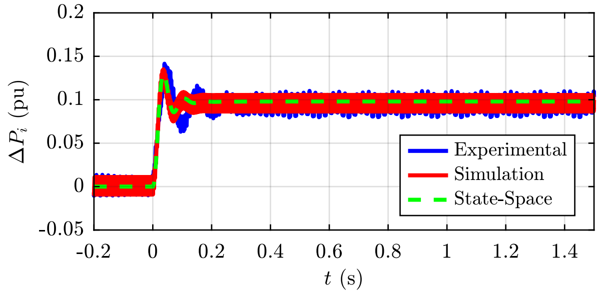

Fig. 5. Inverter power variation to an IM load change in island operation.

case the 0.1 pu IM load step change is applied while both the resistive load and NL load are connected. As it can be observed from both figures, the state–space models almost match the simulated and the experimental responses of the system in both operating conditions.

V. EIGENVALUE–BASED STABILITY ANALYSIS

A. Grid–Connected Operation

The eigenvalues map of the system in grid–connected operation is illustrated in the complex plane in Fig. 6. The system has 25 eigenvalues. They have been calculated considering the converter operating at the nominal power. To clearly define which state variable is related to the eigenvalues, a modal analysis is performed, by calculating the participation factors [6], [25]. The results of the modal analysis are listed below:

- The eigenvalues from 1 to 6 are linked to the dynamic of the LCL filter. From the point of view of the LCL filter block, the loads are ideal current sources connected at the PCC. Therefore, a high–value shunt resistor R_s is inserted at the PCC for the electrotechnical compatibility [24], [27]. The eigenvalues 1 and 2 depend on R_s. As demonstrated in [24], it does not influence the stability;
- The eigenvalues from 7 to 10, 13 and 14 depend on the digital current control. In particular, eigenvalues 7 and 8 are linked to the delay introduced by the digital control (i.e., sampling time), while eigenvalues 9, 10, 13 and 14 are related to the integrators of the PI current control;
- The eigenvalues associated to the NL load are 11 and 12;
- The IM load is related to the eigenvalues from 17 to 21;
- The eigenvalues 15, 16 and from 22 to 25 are linked to the electromechanical part of the S–VSC (i.e., electrical equations, swing equation and excitation control).

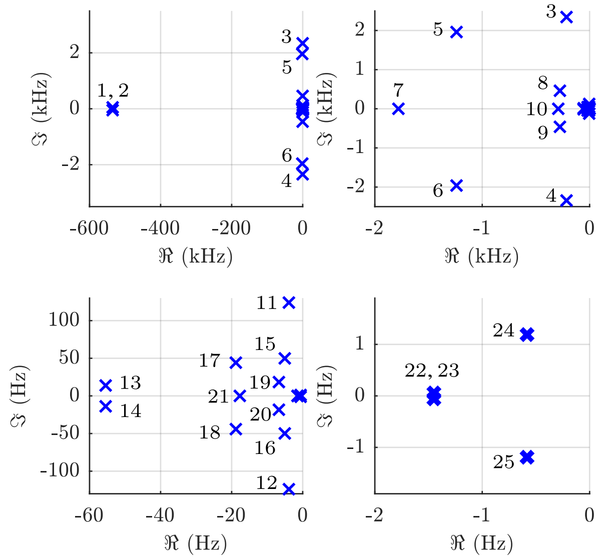

Fig. 6. Eigenvalues map of the system in grid–connected operation.

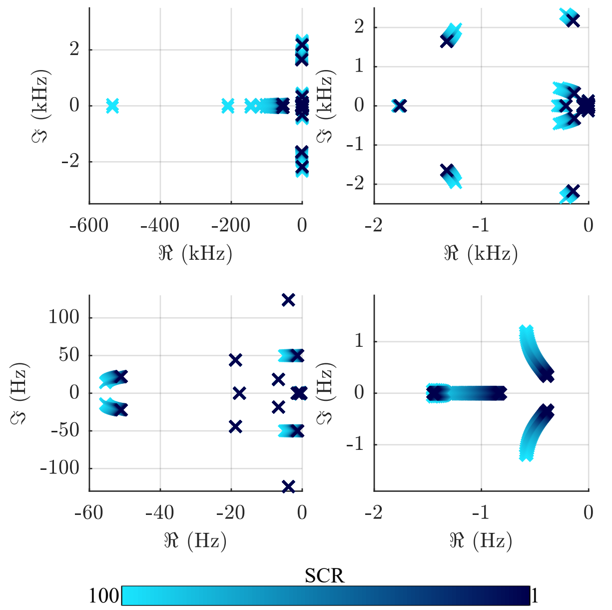

Fig. 7. Eigenvalues map of the system in grid–connected operation varying the SCR from 100 to 1. The color change shows how the eigenvalues move.

Finally, the Short Circuit Ratio (SCR) is changed to study how different grid conditions affect the control stability. Fig. 7 shows how the eigenvalues move if the SCR decreases from the nominal value of 100 (stiff grid condition) to 1 (very weak grid condition). It can be observed that all the eigenvalues linked to the grid inductance (i.e., LCL filter, electrical equation block, excitation control) move from left to right. The conclusion is that the system tends to become unstable if the SCR decreases. However, even under a very weak grid condition, the system is still stable.

This article has been accepted for publication in IEEE Transactions on Industry Applications. This is the author's version which has not been fully edited and content may change prior to final publication. Citation information: DOI 10.1109/TIA.2023.3285523

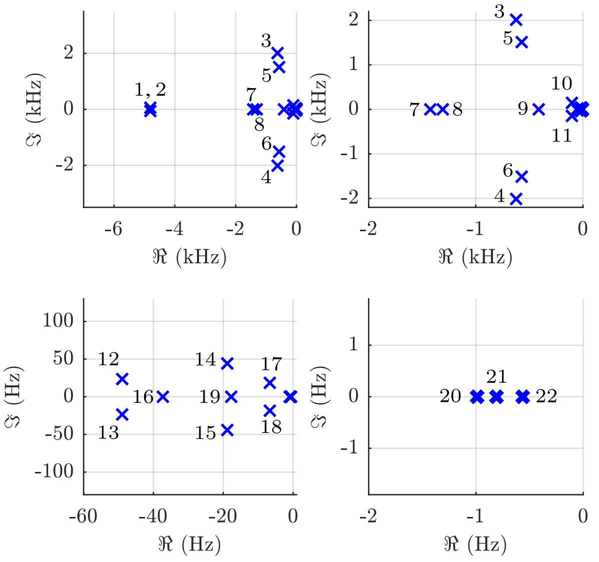

Fig. 8. Eigenvalues map of the system in island operation.

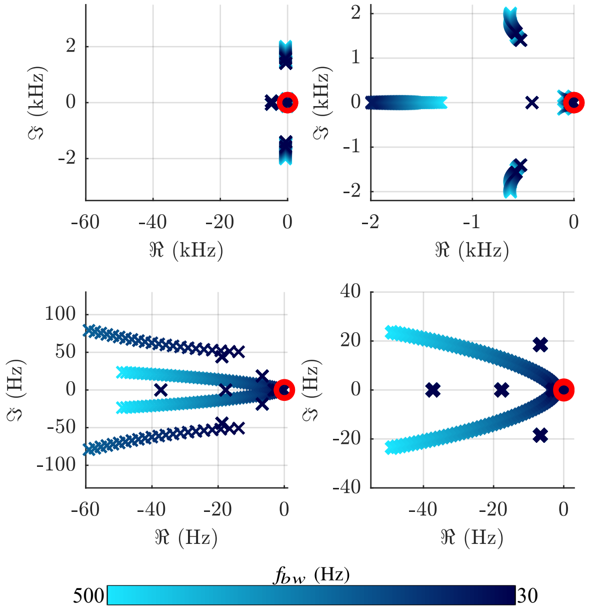

Fig. 9. Eigenvalues map of the system in island operation varying the current control bandwidth f_{bw} from 500 Hz to 30 Hz. The color change shows how the eigenvalues move. The red circle indicate the eigenvalues with positive real part.

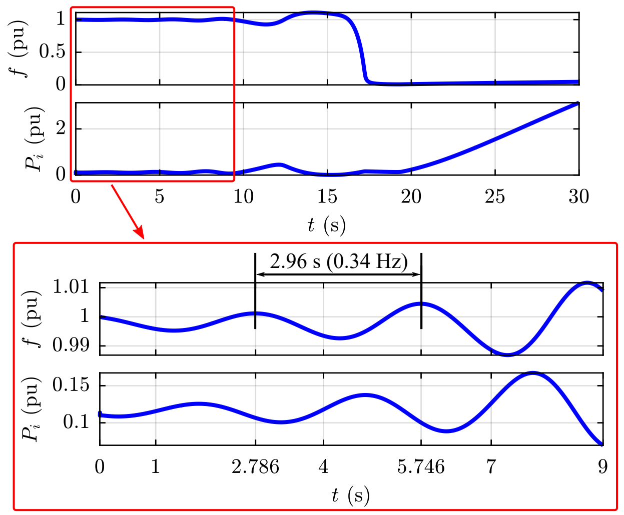

Fig. 10. Instability test to validate the state–space modeling and the eigenvalue analysis. The oscillation frequency is in compliance with the theoretical analysis.

B. Island Operation

The same procedure performed in Section V-A is repeated for the island configuration. In this case the eigenvalues are calculated considering the R load connected and the other two loads disconnected. Fig. 8 shows the eigenvalues map of the system in island–mode in the complex plan. The total number of eigenvalues is 22, because of the lack of the grid. According to the modal analysis:

- As for the grid–connected configuration, the eigenvalues from 1 to 6 are related to the LCL filter;
- The digital current control is associated to the eigenvalues 7, 8, 12 and 13. In particular, eigenvalues 7 and 8 are related to the delay of the digital control, while 12 and 13 are linked to the integrators of the PI current control;
- The eigenvalues 9 and 16 are associated to the NL load;
- The eigenvalues 14, 15, 17–19 are associated to the IM load;
- The electromechanical part of the S–VSC is linked to the eigenvalues 10, 11, 20–22.

To test the validity of the state–space model, the bandwidth of the PI current control f_{bw} is reduced from the nominal value of 500 Hz until an instability condition is reached. As mentioned before, the eigenvalues linked to the integrators of the PI current control are 12 and 13. It can be observed from Fig. 9 that the instability is reached for a bandwidth value of 30 Hz, as the eigenvalues 12 and 13 move to the right half–plane. From the modal analysis, the frequency of the eigenvalues 12 and 13 is equal to 0.34 Hz. Therefore, it is expected that the unstable system oscillates at 0.34 Hz. This analysis has been validated through a PLECS simulation and the result is proposed in Fig. 10. As it can be observed, the oscillations have a period of 2.96 s, which corresponds to almost 0.34 Hz. This corroborates the validity of the state–space modeling procedure and the eigenvalue–based stability analysis.

VI. EXPERIMENTAL VALIDATION

The grid–forming capability of the S–VSC model is validated by means of four experimental tests. The experimental setup is shown in Fig. 11, while its main data are listed in Table I. Its scheme has been already depicted in Fig. 1.

The inverter is supplied by a 15 kW dc–source and controlled by a dSPACE platform. The inverter is connected at the PCC through an LCL filter. Finally, a circuit breaker is located between the PCC and the grid, as shown in Fig. 1 and Fig. 11b. There is no communication between the breaker and

This article has been accepted for publication in IEEE Transactions on Industry Applications. This is the author's version which has not been fully edited and content may change prior to final publication. Citation information: DOI 10.1109/TIA.2023.3285523

TABLE I
MAIN DATA OF THE EXPERIMENTAL SETUP.

Base Values		**Inverter**		**LCL Filter & Grid**	
S_b	15 kVA	S_N	15 kVA	L_f	0.060 pu
V_b	230 $\sqrt{2}$ V	I_N	30 A	R_f	0.006 pu
I_b	30 A	f_{sw}	10 kHz	C_f	0.017 pu
Z_b	10.67 Ω	V_{dc}	650 V	L_{fg}	0.065 pu
f_b	50 Hz			R_{fg}	0.01 pu
ω_b	$2\pi f_b$			L_g	0.001 pu
				R_g	0.00001 pu
Resistive Load		**Induction Machine**		**Non–linear Load**	
P_N	0.1 pu	S_N	0.27 pu	P_N	0.1 pu
		S–VSC Parameters			
R_v	0.02 pu	L_v	0.2 pu	H	4 s
L_{rq}	0.71 pu	R_{rq}	0.01 pu	τ_e	0.1 s

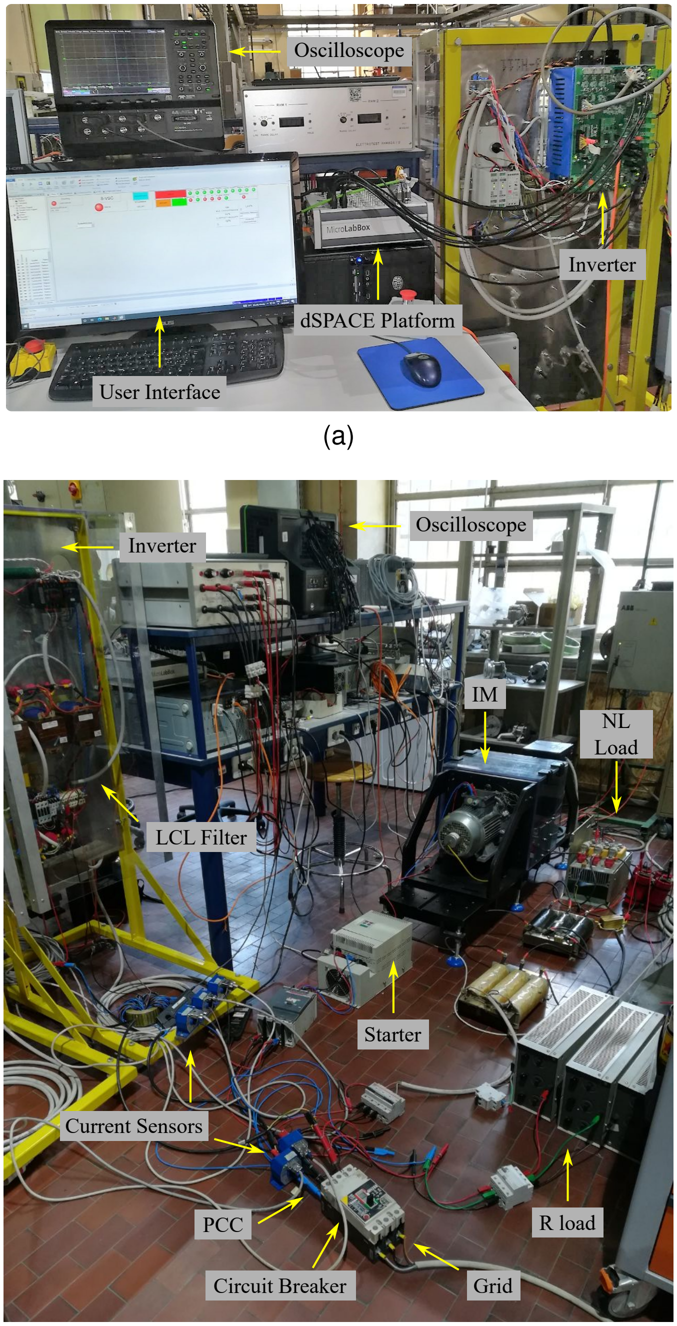

(a)

(b)

Fig. 11. Pictures of the experimental setup.

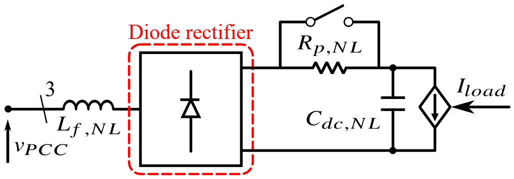

Fig. 12. Scheme of the NL load.

the converter. Consequently, the converter does not receive any information regarding the status of the breaker. Three different loads are located at the PCC to take any typology of load into account: a linear load (R load), a rotating load (IM) and a non–linear load (NL load). They can be connected and disconnected to the system through breakers. The inrush current during the start up of the IM is limited by a starter that is placed between the IM and the PCC, by imposing a maximum slew rate to the supply voltage. Moreover, the IM is loaded by a programmable mechanical load. The NL load consists of a three phase diode rectifier connected at the PCC through a 0.09 pu inductive filter ($L_{f,NL}$) as shown in Fig. 12. At the dc–side, the rectifier is connected to a capacitor bank of 3.3 mF ($C_{dc,NL}$) connected in parallel with an electronic constant current load set to I_{load} = 0.1 pu (ITECH IT 8332 dc electronic load). The capacitor precharge is performed through the soft–start resistor $R_{p,NL}$.

The four experimental tests are the following:

- Test 1: effect of the High Level control. The inverter is connected to the grid. At a certain time, the circuit breaker is opened when only the R load is connected. The test is repeated twice as follows. First, the High Level control is disabled and the system collapses because the frequency and the voltage are not controlled. Next, the High Level control is enabled and the S–VSC provides the power requested by the load and controls the frequency and the voltage of the microgrid. This test highlights the need for the High Level control to make the S–VSC able to operate in grid–forming configuration.
- Test 2: inverter external power references set to 0 pu. The inverter is connected to the grid, the load power is provided by the grid and the inverter is only in charge of the provision of the ancillary services. As soon as the microgrid is islanded (i.e., the circuit breaker is opened) the inverter must immediately supply the loads and follow the load changes with no need of islanding detection.
- Test 3: non–zero inverter external references (e.g., emulating renewable plant generation). Test 2 is repeated with a variable active power reference P_i^{ref} which changes over time simulating the production change of a photovoltaic or wind power plant. As for Test 2, when the microgrid is islanded, the inverter must instantaneously inject the power requested by the loads and follow the loads changes with no need of islanding detection.
- Test 4: fault occurrence during island–mode. The inverter works in grid–forming operation by supplying the R load, the IM load and a programmable load set to an apparent

This article has been accepted for publication in IEEE Transactions on Industry Applications. This is the author's version which has not been fully edited and content may change prior to final publication. Citation information: DOI 10.1109/TIA.2023.3285523

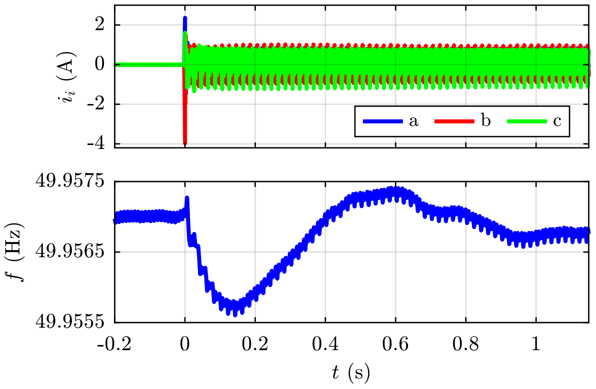

Fig. 13. Grid synchronization and current control enable. From top to bottom: three phase inverter current i_i (A); S–VSC frequency f (Hz).

power of 0.2 pu. At a certain time, the impedance of the programmable load decreases to replicate a symmetric three phase fault. After about 1.6 s, the fault is cleared (i.e., the programmable load is disconnected) and the system returns to the normal operating condition.

Finally, in all tests the speed reference ω_r^* is set to the S–VSC frequency value (pu) after the inverter synchronization procedure (that is, at that instant, the grid frequency value). Similarly, the voltage reference $\widehat{V}_g^*$ is set to the measured voltage amplitude $\widehat{V}_g$ at the end of the synchronization process.

A. Test 1: Effect of the High Level control

Test 1 starts with the circuit breaker closed and the R load connected. The S–VSC synchronizes to the grid with no need of a PLL. As soon as the S–VSC tracks the real grid frequency, the PWM modulation and the current control are enabled, as shown in Fig. 13. At a certain time, the circuit breaker opens to evaluate the effect of the High Level control. If the High Level control is disabled, the S–VSC starts to provide the power requested by the R load. However, the lack of the frequency and voltage control loops leads to the collapse of the frequency and the voltage, as illustrated in Fig. 14. The test is performed with two values of inertia constant H to highlight the effect of the virtual inertia on the frequency decrease, i.e. a larger inertia leads to a slower decrease of the frequency, as happens for a real synchronous machine. Instead, if the High Level control is enabled, the S–VSC can operate as grid–forming by controlling the frequency and the voltage and providing the power requested by the R load, as demonstrated in the same testing conditions proposed in Fig. 14.

B. Test 2: Zero inverter external references

The results of Test 2 are illustrated in Fig. 15, while Table II summarizes the main events. Test 2 is divided into two phases: grid–mode and island operation. During the first part, the circuit breaker is closed, the three loads are connected one by one and their demand is satisfied by the grid. The IM load insertion at $t = 23.3$ s is the same step change shown in Fig. 4. At the beginning of the second part, at $t = 42.53$ s, the circuit breaker suddenly opens without notifications to the control.

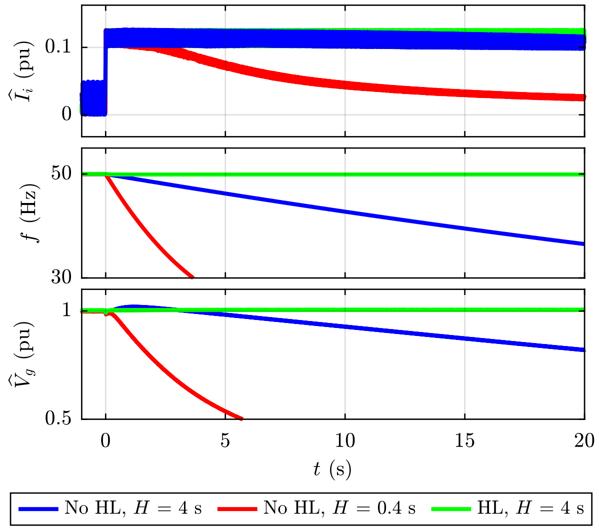

Fig. 14. Island operation with and without the High Level control (HL) for different values of inertia constant H (s). From top to bottom: inverter current amplitude $\widehat{I}_i$ (pu); S–VSC frequency f (Hz); capacitor voltage amplitude $\widehat{V}_g$ (pu).

TABLE II
EVENTS LIST OF TEST 2.

Time (s)	Comment
0	$f \neq 50$ Hz $\Rightarrow P_d^* \neq 0 \Rightarrow P_i \neq 0$.
4.7	R Load insertion $\Rightarrow \Delta P_g = 0.1$ pu.
17.5	IM start up. The starter limits the inrush current.
24	10 Nm IM load insertion $\Rightarrow \Delta P_g = 0.1$ pu.
29.2	NL load precharge.
30.6	Bypass of the soft–start NL load resistance.
36.7	NL load insertion $\Rightarrow \Delta P_g = 0.1$ pu.
42.53	The circuit breaker is opened: Islanding $\Rightarrow$ $\Rightarrow P_g = 0$ pu , $\Delta P_i = 0.3$ pu: the inverter immediately supplies the loads.
49.2	NL load disconnection $\Rightarrow \Delta P_i = -0.1$ pu.
62.2	IM torque inversion from 10 Nm to -10 Nm $\Rightarrow$ $\Rightarrow \Delta P_i = -0.2$ pu: the IM works as a generator and provides almost all the R load power.
70	IM torque load = 0 Nm $\Rightarrow \Delta P_i = 0.1$ pu: the inverter provides the power requested by the loads.
74	IM disconnection.
84.5	NL load precharge.
85.8	Bypass of the soft–start NL load resistance.
90.6	NL load insertion $\Rightarrow \Delta P_i = 0.1$ pu.
103.8	IM start up. The starter limits the inrush current.
110.6	10 Nm IM load insertion $\Rightarrow \Delta P_i = 0.1$ pu.
114.3	IM torque load = 0 Nm $\Rightarrow \Delta P_i = -0.1$ pu.

As it can be noted in Fig. 16, the S–VSC seamlessly provides the power requested by the loads without requiring any kind of communication system. As the capacitor voltage reduces from the grid–mode to the island operation, the total amount of load power decreases as well. Next, the converter correctly follows the load changes over time. The IM load insertion at $t = 110.6$ s is the same step change shown in Fig. 5.

Finally, Fig. 17 shows the measured line to line voltage $v_{g,ab}$ and the current $i_{fg,a}$ in island operation under two different conditions: all loads connected (Fig. 17a); the non–linear load is not connected (Fig. 17b), where it is evident that the NL load introduces a non–negligible harmonic distortion. In the first case (i.e., Fig. 17a) the Total Harmonic Distortion

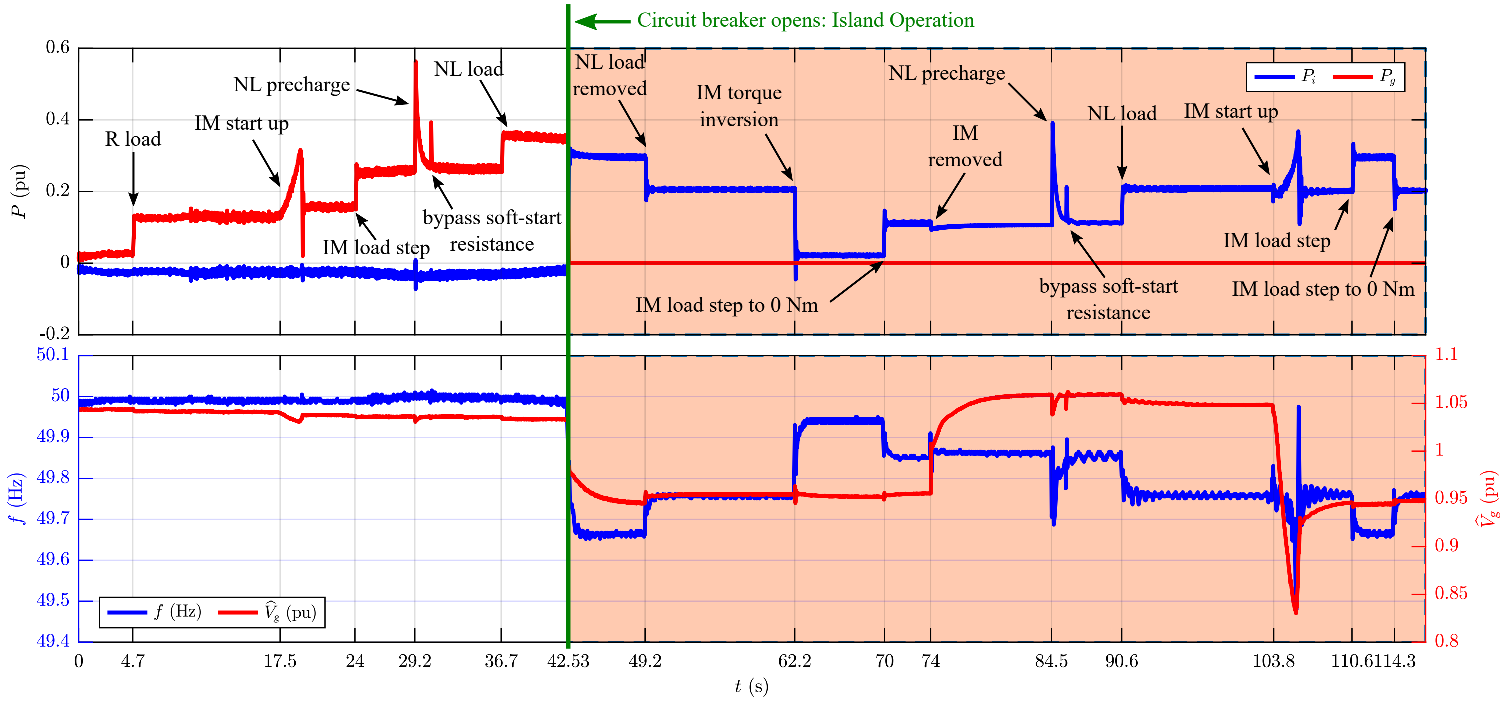

Fig. 15. Results of Test 2: (top) inverter power P_i (pu) and grid power P_g (pu) moving average trends; (bottom) S–VSC frequency f (Hz) and voltage amplitude $\widehat{V}_g$ (pu) trends.

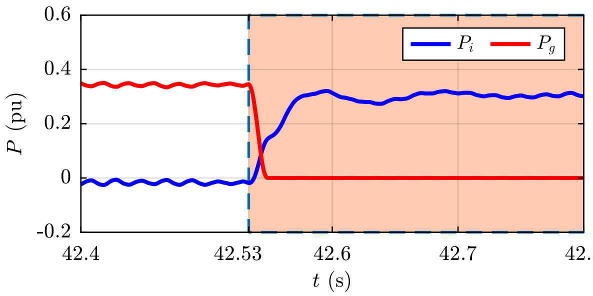

Fig. 16. Transition from grid–mode to island operation in Test 2: inverter power P_i (pu) and grid power P_g (pu) moving average trends.

(THD) of the current is equal to 7.70%, while the THD of the voltage is 3.53%. The main distortion contributions are on the 5th, 7th, 11th and 13th harmonic orders, as the NL load consists of a diode rectifier. Next, in the second case (i.e., Fig. 17b), the THDs are equal to 2.80% and 1.44%, respectively. Finally, Fig. 17 highlights a key feature of the S–VSC model: the S–VSC imposes the current and not the voltage, even in island operation. Indeed, the load current strongly affects the voltage distortion.

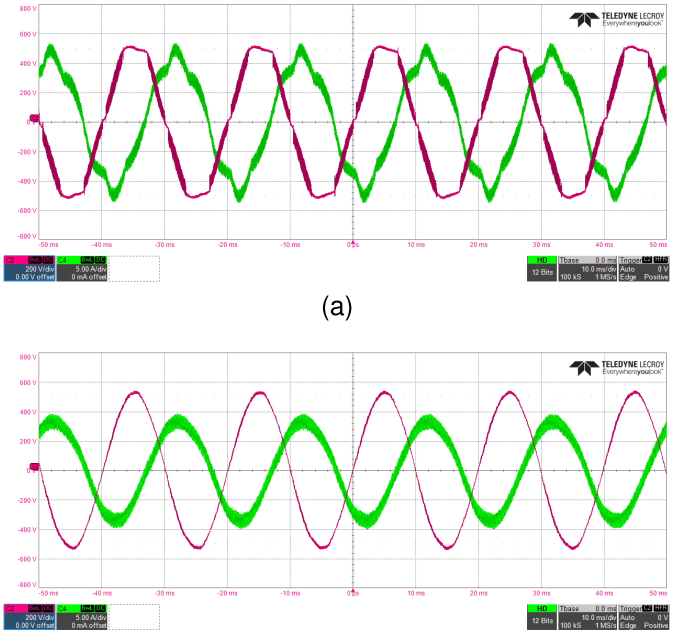

(a)

(b)

Fig. 17. Line to line voltage $v_{g,ab}$ and current $i_{f\,g,a}$ waveforms during island operation: (a) with all loads connected; (b) without the NL load.

C. Test 3: Non–zero inverter external references

Fig. 18 shows the results of Test 3. The comments of the main events of the test are listed in Table III. As for Test 2, Test 3 is divided into two parts: grid–connected and island operation. In the first part, the inverter external reference P_i^{ref} changes over time. The loads are inserted one by one and their demand is satisfied by both the grid and the inverter or only by the inverter, if sufficient. For instance, at t = 33.7 s part of the loads power is provided by the inverter and the remaining contribution comes from the grid. Differently, at t = 49 s, the total amount of the loads demand is satisfied by the inverter. Next, at t = 58.44 s, the circuit breaker opens and the inverter autonomously decreases its injected power, even if the external

This article has been accepted for publication in IEEE Transactions on Industry Applications. This is the author's version which has not been fully edited and content may change prior to final publication. Citation information: DOI 10.1109/TIA.2023.3285523

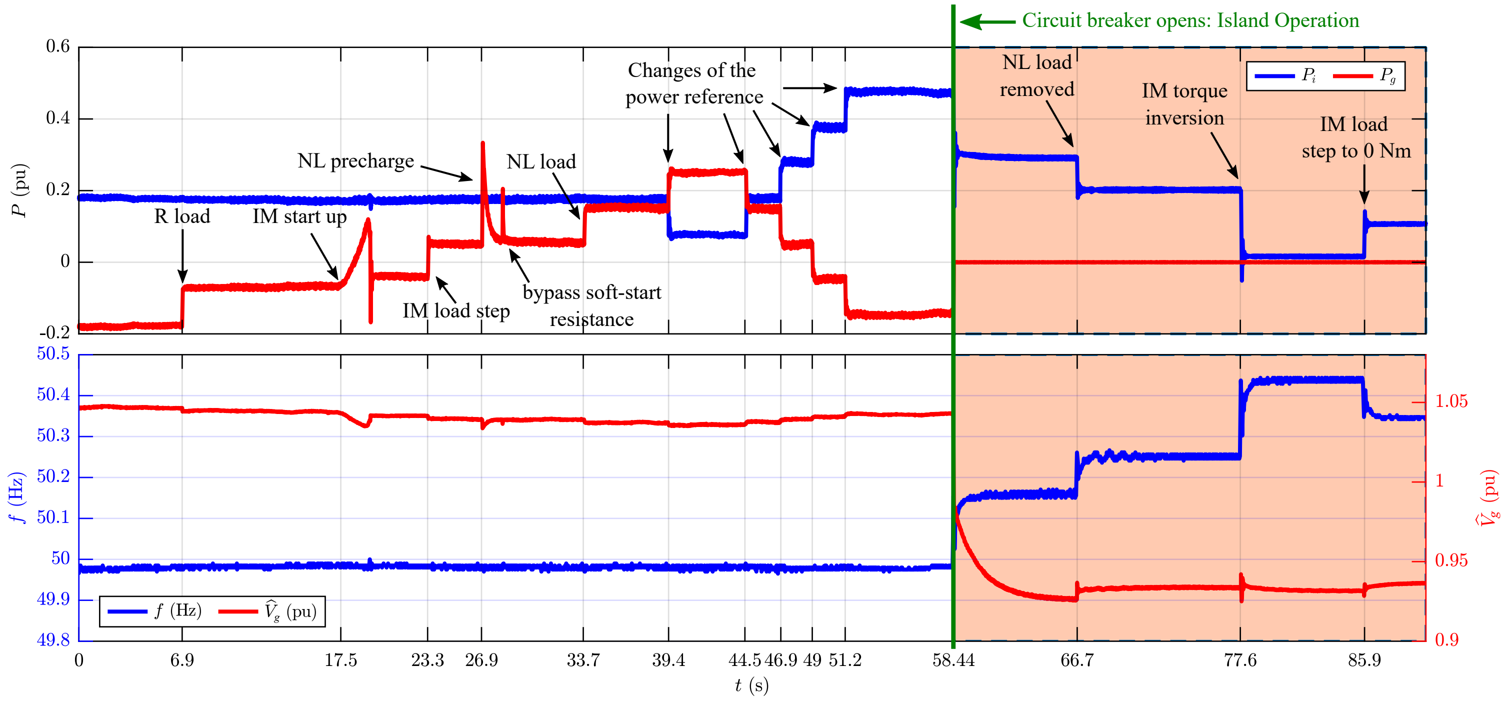

Fig. 18. Results of Test 3: (top) inverter power P_i (pu) and grid power P_g (pu) moving average trends; (bottom) S–VSC frequency f (Hz) and voltage amplitude $\widehat{V}_g$ (pu) trends.

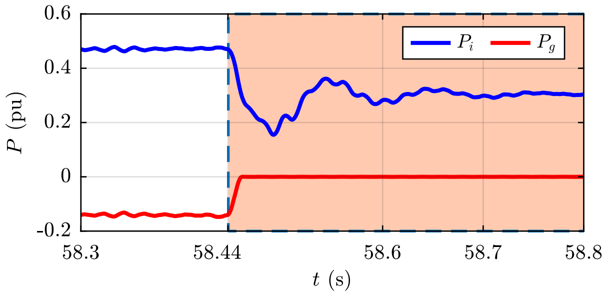

Fig. 19. Transition from grid–mode to island operation in Test 3: inverter power P_i (pu) and grid power P_g (pu) moving average trends.

TABLE III
EVENTS LIST OF TEST 3.

Time (s)	Comment
0	$P_i^{ref} = 0.2$ pu. The inverter injects power into the grid. $f \neq 50$ Hz $\Rightarrow P_d^* \neq 0 \Rightarrow P_i^* = P_d^* + P_i^{ref}$.
6.9	R Load insertion $\Rightarrow \Delta P_g = 0.1$ pu. The inverter satisfies the R load request and the remaing power is injected into the grid.
17.5	IM start up. The starter limits the inrush current.
23.3	10 Nm IM load insertion $\Rightarrow \Delta P_g = 0.1$ pu. The inverter provides part of the loads power. The remaing contribution is guaranteed by the grid.
26.9	NL load precharge.
28.3	Bypass of the soft–start NL load resistance.
33.7	NL load insertion $\Rightarrow \Delta P_g = 0.1$ pu. The inverter and the grid almost equally provide the loads power.
39.4	Inverter reference step $\Delta P_i^{ref} = -0.1$ pu $\Rightarrow$ $\Rightarrow \Delta P_g = 0.1$ pu.
44.5	Inverter reference step $\Delta P_i^{ref} = 0.1$ pu $\Rightarrow$ $\Rightarrow \Delta P_g = -0.1$ pu.
46.9	Inverter reference step $\Delta P_i^{ref} = 0.1$ pu $\Rightarrow$ $\Rightarrow \Delta P_g = -0.1$ pu.
49	Inverter reference step $\Delta P_i^{ref} = 0.1$ pu $\Rightarrow$ $\Rightarrow \Delta P_g = -0.1$ pu. The inverter provides all the power requested by the loads and the remaining term is injected into the grid.
51.2	Inverter reference step $\Delta P_i^{ref} = 0.1$ pu $\Rightarrow$ $\Rightarrow \Delta P_g = -0.1$ pu.
58.44	The circuit breaker is opened: Islanding $\Rightarrow P_g = 0$ pu. The inverter immediately provides only the loads power.
66.7	NL load disconnection $\Rightarrow \Delta P_i = -0.1$ pu.
77.6	IM torque inversion from 10 Nm to -10 Nm $\Rightarrow$ $\Rightarrow \Delta P_i = -0.2$ pu: the IM works as a generator and provides almost all the R load power.
85.9	IM torque load = 0 Nm $\Rightarrow \Delta P_i = 0.1$ pu: The inverter provides the power requested by the loads.

reference does not change, as for the curtailment operation. Indeed, in such condition, the converter can only inject the power requested by the loads. If a storage system was added, the surplus of power could be used to charge it. Even in this case, there is no communication between the converter and the grid. Therefore, the converter seamlessly provides the power requested by the loads, as shown in Fig. 19. Finally, as in Test 2, the converter properly follows the loads changes.

D. Test 4: Fault occurrence in island operation

The results of Test 4 are shown in Fig. 20 and Fig. 21. At t = 0 s, the fault causes a voltage dip of about 0.35 pu. During the fault, the inverter does not trip and feeds the microgrid loads. The frequency decreases and the inverter current is saturated at the limit of 0.8 pu (imposed by the user). As soon as the fault is cleared, the frequency and the voltage are restored to the normal operating values and the inverter supplies the

This article has been accepted for publication in IEEE Transactions on Industry Applications. This is the author's version which has not been fully edited and
content may change prior to final publication. Citation information: DOI 10.1109/TIA.2023.3285523

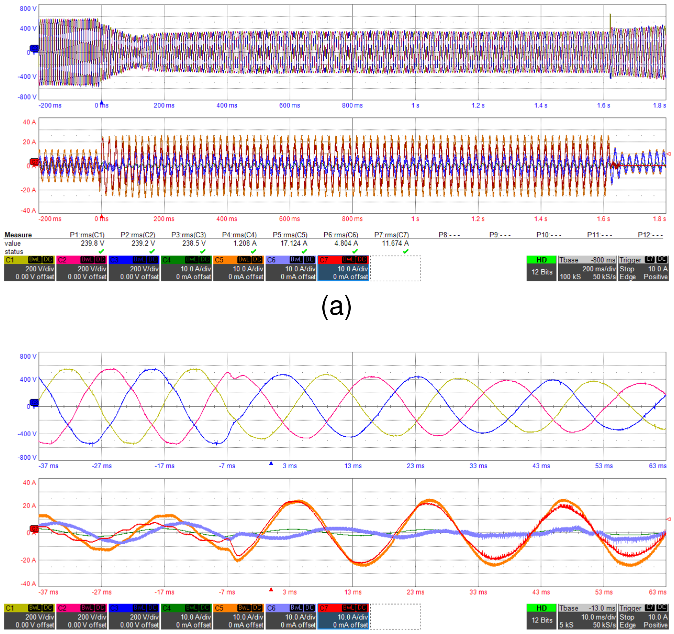

(a)

(b)

Fig. 20. Results of Test 4. C1, C2 and C3 are the line to line three phase voltages $v_{g,ll}$. C4 is the R load current $i_{R,a}$, C5 is the inverter current $i_{i,a}$, C6 is the IM current $i_{IM,a}$ and C7 is the fault current $i_{F,a}$. The RMS values are calculated in the time range from 200 ms to 1.6 s. From top to bottom: (a) entire fault; (b) zoom at the beginning of the fault.

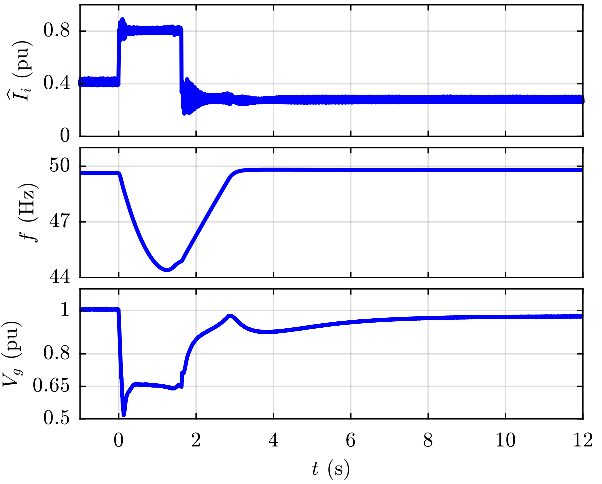

Fig. 21. Results of Test 4. From top to bottom: inverter current amplitude $\widehat{I}_i$ (pu); S–VSC frequency f (Hz); capacitor voltage amplitude $\widehat{V}_g$ (pu).

loads. This test validates the robustness of the proposed control algorithm against a fault, as the microgrid does not collapse during the fault and, as soon as the fault is cleared, the S–VSC restores the pre–fault normal operating condition.

VII. CONCLUSION

The concept of Virtual Synchronous Machine represents a promising solution to mitigate the future power system inertia reduction and the associated grid frequency and voltage stability concerns. Moreover, the penetration of distributed renewable energy sources together with the resiliency of the grid can be enhanced by the diffusion of microgrids able to provide ancillary services and work both in grid–connected and island configuration. This paper proposed an S–VSC model which can operate both as in grid–following and in grid–forming modes, without affecting the compensator performance already described in previous papers. The eigenvalue stability analysis proved theoretically that the proposed solution is stable in both grid–connected and islanded mode. These findings have been validated experimentally on a microgrid, including different load typologies (passive linear, non–linear and active loads, such as line fed motors). As soon as the microgrid is islanded, the S–VSC provides the power requested by the loads, demonstrating its suitability for the control of inverter–based microgrids. Moreover, the tests show how the S–VSC seamlessly moves from the grid–following to the island operation with no need of communication between the grid and the converter. Finally, an experimental test demonstrates that the S–VSC can operate in island–mode even in case of a fault occurrence, thus demonstrating the robustness of a microgrid controlled according to the proposed solution. Future work will focus on integrating a feedback of the grid connection status in the inverter control. This would make the converter able to re-synchronize to the grid after the island operation. Moreover, more studies on integrating the secondary frequency and voltage control during the island operation will be carried out. Another future step will expand the microgrid with more converters.

APPENDIX A
STATE–SPACE MODELS

In the following, for the generic quantity γ, the term $\Delta\gamma^{dq}$ stands for the row vector $[\Delta\gamma^d, \Delta\gamma^q]$, where $\Delta\gamma^d$ and $\Delta\gamma^q$ are respectively the d–component and the q–component of $\Delta\gamma$ in the (d,q) reference frame rotating at the virtual speed ω_r.

A. Loads

1) Resistive Load:

$$\begin{cases} \dfrac{d\mathbf{x_R}}{dt} & = & \mathbf{A_R x_R} + \mathbf{B_R u_R} \\ \mathbf{y_R} & = & \mathbf{C_R x_R} + \mathbf{D_R u_R} \end{cases} \tag{21}$$

$$\mathbf{u_R} = \left[\Delta v^{dq}_{pcc}, P_{load}\right]^{\mathrm{T}}, \mathbf{y_R} = \left[\Delta i^{dq}_R\right]^{\mathrm{T}} \tag{22}$$

$$\mathbf{x_R} = 0, \mathbf{A_R} = 0, \mathbf{B_R} = [0]^{1\mathrm{x}3}, \mathbf{C_R} = [0]^{2\mathrm{x}1} \tag{23}$$

$$\mathbf{D_R} = \begin{bmatrix} \dfrac{1}{R_R} & 0 & 0 \\ 0 & \dfrac{1}{R_R} & \dfrac{V^q_{pcc0}}{R_R} \end{bmatrix} \tag{24}$$

where R_R is the resistance of the load, i_R is the load current and P_{load} is a logic flag to emulate the connection or disconnection of the load.

2) Induction Machine:

$$\begin{cases} \dfrac{d\mathbf{x_{IM}}}{dt} &= \mathbf{A_{IM}}\mathbf{x_{IM}} + \mathbf{B_{IM}}\mathbf{u_{IM}} \\ \mathbf{y_{IM}} &= \mathbf{C_{IM}}\mathbf{x_{IM}} + \mathbf{D_{IM}}\mathbf{u_{IM}} \end{cases} \tag{25}$$

$$\mathbf{x_{IM}} = \left[\Delta\lambda_s^{dq}, \Delta\lambda_r^{dq}, \Delta\omega_{IM}\right]^{\mathrm{T}} \tag{26}$$

$$\mathbf{u_{IM}} = \left[\Delta v_{pcc}^{dq}, \Delta\omega, \Delta T_L\right]^{\mathrm{T}} \tag{27}$$

$$\mathbf{y_{IM}} = \left[\Delta i_s^{dq}\right]^{\mathrm{T}} \tag{28}$$

where λ_s is the stator flux, λ_r is the rotor flux, ω_{IM} is the rotor speed, T_L is the load torque, i_s is the stator current and ω is the grid frequency ω_g in grid–mode operation and the virtual frequency ω_r in island operation. The state–space matrices can be found in [28].

3) Non–linear load:

$$\begin{cases} \dfrac{d\mathbf{x_{NL}}}{dt} &= \mathbf{A_{NL}}\mathbf{x_{NL}} + \mathbf{B_{NL}}\mathbf{u_{NL}} \\ \mathbf{y_{NL}} &= \mathbf{C_{NL}}\mathbf{x_{NL}} + \mathbf{D_{NL}}\mathbf{u_{NL}} \end{cases} \tag{29}$$

$$\mathbf{x_{NL}} = \left[\Delta i_{dc,NL}, \Delta v_{NL}\right]^{\mathrm{T}} \tag{30}$$

$$\mathbf{u_{NL}} = \left[\Delta v_{pcc}^{dq}, \Delta I_{load}\right]^{\mathrm{T}} \tag{31}$$

$$\mathbf{y_{NL}} = \left[\Delta i_{dc,NL}, \Delta v_{NL}, \Delta i_{NL}^{q}\right]^{\mathrm{T}} \tag{32}$$

The state–space representation refers to the average model of a three phase diode rectifier [29] connected to a capacitor in parallel with a constant current load. The rectifier is connected at the PCC trough an inductive filter with inductance $L_{f,NL}$. $i_{dc,NL}$ is the dc current of the rectifier, v_{NL} is the voltage of the capacitor on the dc–side of the rectifier, I_{load} is the load current and i_{NL}^{q} is the q–component of the ac rectifier current. The state–space matrices are retrieved from [29].

B. LCL Filter

The LCL filter has a damping resistance R_d. The capacitor voltage is v_c, while the measured voltage v_g is the sum of v_c and the voltage drop on R_d. The subscript "LCL,G" refers to the state–space representation of the LCL filter in grid–connected operation, while the subscript "LCL,I" refers to the island–mode.

1) Grid–mode:

$$\begin{cases} \dfrac{d\mathbf{x_{LCL,G}}}{dt} &= \mathbf{A_{LCL,G}}\mathbf{x_{LCL,G}} + \mathbf{B_{LCL,G}}\mathbf{u_{LCL,G}} \\ \mathbf{y_{LCL,G}} &= \mathbf{C_{LCL,G}}\mathbf{x_{LCL,G}} + \mathbf{D_{LCL,G}}\mathbf{u_{LCL,G}} \end{cases} \tag{33}$$

$$\mathbf{x_{LCL,G}} = [\Delta i_i^{dq}, \Delta i_{fg}^{dq}, \Delta i_g^{dq}, \Delta v_c^{dq}]^{\mathrm{T}} \tag{34}$$

$$\mathbf{u_{LCL,G}} = [\Delta e_i^{dq}, \Delta e_g^{dq}, \Delta\omega_r, \Delta i_L^{dq}]^{\mathrm{T}} \tag{35}$$

where i_L is the total load current.

$$\mathbf{y_{LCL,G}} = [\Delta i_i^{dq}, \Delta i_{fg}^{dq}, \Delta i_g^{dq}, \Delta v_g^{dq}, \Delta v_{pcc}^{dq}]^{\mathrm{T}} \tag{36}$$

In the following, R_D, R_F and R_G are equal to, respectively:

$$R_D = R_f + R_d \tag{37}$$

$$R_F = R_d + R_{fg} + R_s \tag{38}$$

$$R_G = R_s + R_g \tag{39}$$

The only non–zero elements of $\mathbf{D_{LCL,G}}$ are:

$$\mathbf{D_{LCL,G}}(9,6) = \mathbf{D_{LCL,G}}(10,7) = -R_s \tag{40}$$

$$\mathbf{A_{LCL,G}} = \begin{bmatrix} -\omega_b\frac{R_D}{L_f} & \omega_{r0}\omega_b & \omega_b\frac{R_d}{L_f} & 0 & 0 & 0 & -\frac{\omega_b}{L_f} & 0 \\ -\omega_{r0}\omega_b & -\omega_b\frac{R_D}{L_f} & 0 & \omega_b\frac{R_d}{L_f} & 0 & 0 & 0 & -\frac{\omega_b}{L_f} \\ \omega_b\frac{R_d}{L_{fg}} & 0 & -\omega_b\frac{R_F}{L_{fg}} & \omega_{r0}\omega_b & \omega_b\frac{R_s}{L_{fg}} & 0 & \frac{\omega_b}{L_{fg}} & 0 \\ 0 & \omega_b\frac{R_d}{L_{fg}} & -\omega_{r0}\omega_b & -\omega_b\frac{R_F}{L_{fg}} & 0 & \omega_b\frac{R_s}{L_{fg}} & 0 & \frac{\omega_b}{L_{fg}} \\ 0 & 0 & \omega_b\frac{R_s}{L_g} & 0 & -\omega_b\frac{R_G}{L_g} & \omega_{r0}\omega_b & 0 & 0 \\ 0 & 0 & 0 & \omega_b\frac{R_s}{L_g} & -\omega_{r0}\omega_b & -\omega_b\frac{R_G}{L_g} & 0 & 0 \\ \frac{\omega_b}{C_f} & 0 & -\frac{\omega_b}{C_f} & 0 & 0 & 0 & 0 & \omega_{r0}\omega_b \\ 0 & \frac{\omega_b}{C_f} & 0 & -\frac{\omega_b}{C_f} & 0 & 0 & -\omega_{r0}\omega_b & 0 \end{bmatrix} \tag{41}$$

$$\mathbf{B_{LCL,G}} = \begin{bmatrix} \frac{\omega_b}{L_f} & 0 & 0 & 0 & \omega_b I_{i0}^{q} & 0 & 0 \\ 0 & \frac{\omega_b}{L_f} & 0 & 0 & -\omega_b I_{i0}^{d} & 0 & 0 \\ 0 & 0 & 0 & 0 & \omega_b I_{fg0}^{q} & \omega_b\frac{R_s}{L_{fg}} & 0 \\ 0 & 0 & 0 & 0 & -\omega_b I_{fg0}^{d} & 0 & \omega_b\frac{R_s}{L_{fg}} \\ 0 & 0 & -\frac{\omega_b}{L_g} & 0 & \omega_b I_{g0}^{q} & -\omega_b\frac{R_s}{L_g} & 0 \\ 0 & 0 & 0 & -\frac{\omega_b}{L_g} & -\omega_b I_{g0}^{d} & 0 & -\omega_b\frac{R_s}{L_g} \\ 0 & 0 & 0 & 0 & \omega_b V_{c0}^{q} & 0 & 0 \\ 0 & 0 & 0 & 0 & -\omega_b V_{c0}^{d} & 0 & 0 \end{bmatrix} \tag{42}$$

$$\mathbf{C_{LCL,G}} = \begin{bmatrix} 1 & 0 & 0 & 0 & 0 & 0 & 0 & 0 \\ 0 & 1 & 0 & 0 & 0 & 0 & 0 & 0 \\ 0 & 0 & 1 & 0 & 0 & 0 & 0 & 0 \\ 0 & 0 & 0 & 1 & 0 & 0 & 0 & 0 \\ 0 & 0 & 0 & 0 & 1 & 0 & 0 & 0 \\ 0 & 0 & 0 & 0 & 0 & 1 & 0 & 0 \\ R_d & 0 & -R_d & 0 & 0 & 0 & 1 & 0 \\ 0 & R_d & 0 & -R_d & 0 & 0 & 0 & 1 \\ 0 & 0 & R_s & 0 & -R_s & 0 & 0 & 0 \\ 0 & 0 & 0 & R_s & 0 & -R_s & 0 & 0 \end{bmatrix} \tag{43}$$

2) Island–mode:

$$\begin{cases} \dfrac{d\mathbf{x_{LCL,I}}}{dt} & = \mathbf{A_{LCL,I}x_{LCL,I}} + \mathbf{B_{LCL,I}u_{LCL,I}} \\ \mathbf{y_{LCL,I}} & = \mathbf{C_{LCL,I}x_{LCL,I}} + \mathbf{D_{LCL,I}u_{LCL,I}} \end{cases} \tag{44}$$

$$\mathbf{x_{LCL,I}} = [\Delta i_i^{dq}, \Delta i_{fg}^{dq}, \Delta v_c^{dq}]^{\mathrm{T}} \tag{45}$$

$$\mathbf{u_{LCL,I}} = [\Delta e_i^{dq}, \Delta\omega_r, \Delta i_L^{dq}]^{\mathrm{T}} \tag{46}$$

$$\mathbf{y_{LCL,I}} = [\Delta i_i^{dq}, \Delta i_{fg}^{dq}, \Delta v_g^{dq}, \Delta v_{pcc}^{dq}]^{\mathrm{T}} \tag{47}$$

$$\mathbf{A_{LCL,I}} =$$

$$\begin{bmatrix} -\omega_b \dfrac{R_D}{L_f} & \omega_{r0}\omega_b & \omega_b \dfrac{R_d}{L_f} & 0 & -\dfrac{\omega_b}{L_f} & 0 \\ -\omega_{r0}\omega_b & -\omega_b \dfrac{R_D}{L_f} & 0 & \omega_b \dfrac{R_d}{L_f} & 0 & -\dfrac{\omega_b}{L_f} \\ \omega_b \dfrac{R_d}{L_{fg}} & 0 & -\omega_b \dfrac{R_F}{L_{fg}} & \omega_{r0}\omega_b & \dfrac{\omega_b}{L_{fg}} & 0 \\ 0 & \omega_b \dfrac{R_d}{L_{fg}} & -\omega_{r0}\omega_b & -\omega_b \dfrac{R_F}{L_{fg}} & 0 & \dfrac{\omega_b}{L_{fg}} \\ \dfrac{\omega_b}{C_f} & 0 & -\dfrac{\omega_b}{C_f} & 0 & 0 & \omega_{r0}\omega_b \\ 0 & \dfrac{\omega_b}{C_f} & 0 & -\dfrac{\omega_b}{C_f} & -\omega_{r0}\omega_b & 0 \end{bmatrix} \tag{48}$$

$$\mathbf{B_{LCL,I}} = \begin{bmatrix} \dfrac{\omega_b}{L_f} & 0 & \omega_b I_{i0}^q & 0 & 0 \\ 0 & \dfrac{\omega_b}{L_f} & -\omega_b I_{i0}^d & 0 & 0 \\ 0 & 0 & \omega_b I_{fg0}^q & \omega_b \dfrac{R_s}{L_{fg}} & 0 \\ 0 & 0 & -\omega_b I_{fg0}^d & 0 & \omega_b \dfrac{R_s}{L_{fg}} \\ 0 & 0 & \omega_b V_{c0}^q & 0 & 0 \\ 0 & 0 & -\omega_b V_{c0}^d & 0 & 0 \end{bmatrix} \tag{49}$$

$$\mathbf{C_{LCL,I}} = \begin{bmatrix} 1 & 0 & 0 & 0 & 0 & 0 \\ 0 & 1 & 0 & 0 & 0 & 0 \\ 0 & 0 & 1 & 0 & 0 & 0 \\ 0 & 0 & 0 & 1 & 0 & 0 \\ R_d & 0 & -R_d & 0 & 1 & 0 \\ 0 & R_d & 0 & -R_d & 0 & 1 \\ 0 & 0 & R_s & 0 & 0 & 0 \\ 0 & 0 & 0 & R_s & 0 & 0 \end{bmatrix} \tag{50}$$

The only non–zero elements of $\mathbf{D_{LCL,I}}$ are:

$$\mathbf{D_{LCL,I}}(7,4) = \mathbf{D_{LCL,I}}(8,5) = -R_s \tag{51}$$

C. Inverter

The Inverter block is the same proposed in [25] and it is not reported here.

D. S–VSC Control

The S–VSC control block consists of the Electrical Equations block and the power loops block (i.e., Mechanical Emulation and Excitation Control). The former is the same proposed in [25] and it is not reported here. The latter is slightly different from [25] and it is proposed in the following.

The power loops block changes according to the operating configuration (i.e., grid–mode or island). In the following, f_p and f_q define if the droop references P_d^* and Q_d^* are applied on the inverter references or on the virtual references, are explained in Section III and shown in Fig. 3 with the switch K_{sw}.

1) Grid–mode:

$$\begin{cases} \dfrac{d\mathbf{x_{PW,G}}}{dt} & = \mathbf{A_{PW,G}x_{PW,G}} + \mathbf{B_{PW,G}u_{PW,G}} \\ \mathbf{y_{PW,G}} & = \mathbf{C_{PW,G}x_{PW,G}} + \mathbf{D_{PW,G}u_{PW,G}} \end{cases} \tag{52}$$

$$\mathbf{x_{PW,G}} = [\Delta\omega_r, \Delta\delta, \Delta\lambda_e]^{\mathrm{T}} \tag{53}$$

where δ is the angle difference between the virtual rotor angle θ_r and the grid voltage angle θ_g.

$$\mathbf{u_{PW,G}} = \Big[\Delta P_v^{ref}, \Delta Q_v^{ref}, \Delta P_d^*, \Delta Q_d^*, \\ \Delta v_g^{dq}, \Delta i_v^{dq}, \Delta\omega_g\Big]^{\mathrm{T}} \tag{54}$$

$$\mathbf{y_{PW,G}} = [\Delta P_v, \Delta Q_v, \Delta\omega_r, \Delta\delta, \Delta\lambda_e]^{\mathrm{T}} \tag{55}$$

$$\mathbf{A_{PW,G}} = \begin{bmatrix} 0 & 0 & 0 \\ \omega_b & 0 & 0 \\ 0 & 0 & 0 \end{bmatrix} \tag{56}$$

$$\mathbf{B_{PW,G}} = \begin{bmatrix} \dfrac{1}{2H} & 0 & \dfrac{f_p}{2H} & 0 & -\dfrac{I_{v0}^d}{2H} & -\dfrac{I_{v0}^q}{2H} & -\dfrac{V_{g0}^d}{2H} & -\dfrac{V_{g0}^q}{2H} & 0 \\ 0 & 0 & 0 & 0 & 0 & 0 & 0 & 0 & -\omega_b \\ 0 & k_e \dfrac{1}{V_{g0}} & 0 & k_e \dfrac{f_q}{V_{g0}} & k_e \dfrac{I_{v0}^q}{V_{g0}} & -k_e \dfrac{I_{v0}^d}{V_{g0}} & -k_e \dfrac{V_{g0}^q}{V_{g0}} & k_e \dfrac{V_{g0}^d}{V_{g0}} & 0 \end{bmatrix} \tag{57}$$

$$\mathbf{C_{PW,G}} = \begin{bmatrix} 0 & 0 & 0 \\ 0 & 0 & 0 \\ 1 & 0 & 0 \\ 0 & 1 & 0 \\ 0 & 0 & 1 \end{bmatrix} \tag{58}$$

$$\mathbf{D_{PW,G}} = \begin{bmatrix} 0 & 0 & 0 & 0 & I_{v0}^{d} & I_{v0}^{q} & V_{g0}^{d} & V_{g0}^{q} & 0 \\ 0 & 0 & 0 & 0 & -I_{v0}^{q} & I_{v0}^{d} & V_{g0}^{q} & -V_{g0}^{d} & 0 \\ 0 & 0 & 0 & 0 & 0 & 0 & 0 & 0 & 0 \\ 0 & 0 & 0 & 0 & 0 & 0 & 0 & 0 & 0 \\ 0 & 0 & 0 & 0 & 0 & 0 & 0 & 0 & 0 \end{bmatrix} \tag{59}$$

In (57) H is the inertia constant in seconds and k_e is the gain of the excitation control (pu) [20].

2) Island–mode:

$$\begin{cases} \dfrac{d\mathbf{x_{PW,I}}}{dt} & = & \mathbf{A_{PW,I}x_{PW,I}} + \mathbf{B_{PW,I}u_{PW,I}} \\ \mathbf{y_{PW,I}} & = & \mathbf{C_{PW,I}x_{PW,I}} + \mathbf{D_{PW,I}u_{PW,I}} \end{cases} \tag{60}$$

$$\mathbf{x_{PW,I}} = [\Delta\omega_r, \Delta\lambda_e]^{\mathrm{T}} \tag{61}$$

$$\mathbf{u_{PW,I}} = \left[\Delta P_v^{ref}, \Delta Q_v^{ref}, \Delta P_d^*, \Delta Q_d^*, \Delta v_g^{dq}, \Delta i_v^{dq}\right]^{\mathrm{T}} \tag{62}$$

$$\mathbf{y_{PW,I}} = [\Delta P_v, \Delta Q_v, \Delta\omega_r, \Delta\lambda_e]^{\mathrm{T}} \tag{63}$$

$$\mathbf{A_{PW,I}} = [0]^{2\mathrm{x}2} \tag{64}$$

$$\mathbf{B_{PW,I}} = \begin{bmatrix} \dfrac{1}{2H} & 0 & \dfrac{f_p}{2H} & 0 & -\dfrac{I_{vd0}}{2H} & -\dfrac{I_{v0}^{q}}{2H} & -\dfrac{V_{g0}^{d}}{2H} & -\dfrac{V_{g0}^{q}}{2H} & 0 \\ 0 & k_e\dfrac{1}{V_{g0}} & 0 & k_e\dfrac{f_q}{V_{g0}} & k_e\dfrac{I_{vq0}}{V_{g0}} & -k_e\dfrac{I_{v0}^{d}}{V_{g0}} & -k_e\dfrac{V_{g0}^{q}}{V_{g0}} & k_e\dfrac{V_{g0}^{d}}{V_{g0}} & 0 \end{bmatrix} \tag{65}$$

$$\mathbf{C_{PW,I}} = \begin{bmatrix} 0 & 0 \\ 0 & 0 \\ 1 & 0 \\ 0 & 1 \end{bmatrix} \tag{66}$$

$$\mathbf{D_{PW,I}} = \begin{bmatrix} 0 & 0 & 0 & 0 & I_{v0}^{d} & I_{v0}^{q} & V_{g0}^{d} & V_{g0}^{q} \\ 0 & 0 & 0 & 0 & -I_{v0}^{q} & I_{v0}^{d} & V_{g0}^{q} & -V_{g0}^{d} \\ 0 & 0 & 0 & 0 & 0 & 0 & 0 & 0 \\ 0 & 0 & 0 & 0 & 0 & 0 & 0 & 0 \end{bmatrix} \tag{67}$$

E. Reference Calculation

$$\mathbf{u_{Ref}} = \left[\Delta P_i^{ref}, \Delta Q_i^{ref}, \Delta i_v^{dq}, \Delta P_d^*, \Delta Q_d^*, \Delta v_g^{dq}\right]^{\mathrm{T}} \tag{68}$$

$$\mathbf{x_{Ref}} = 0, \mathbf{y_{Ref}} = \left[\Delta i^{*,dq}\right]^{\mathrm{T}} \tag{69}$$

$$\mathbf{A_{Ref}} = 0, \mathbf{B_{Ref}} = [0]^{1\mathrm{x}8}, \mathbf{C_{Ref}} = [0]^{2\mathrm{x}1} \tag{70}$$

$$\mathbf{D_{Ref}} = \begin{bmatrix} \dfrac{V_{g0}^{d}}{V_{g0}^{2}} & \dfrac{V_{g0}^{q}}{V_{g0}^{2}} & 1 & 0 & (1-f_p)\dfrac{V_{g0}^{d}}{V_{g0}^{2}} & (1-f_q)\dfrac{V_{g0}^{q}}{V_{g0}^{2}} & \dfrac{P_{i0}^*(V_{g0}^{2,q}-V_{g0}^{2,d})-2Q_{i0}^*V_{g0}^{d}V_{g0}^{q}}{V_{g0}^{4}} & \dfrac{Q_{i0}^*(V_{g0}^{2,d}-V_{g0}^{2,q})-2P_{i0}^*V_{g0}^{d}V_{g0}^{q}}{V_{g0}^{4}} \\ \dfrac{V_{g0}^{q}}{V_{g0}^{2}} & -\dfrac{V_{g0}^{d}}{V_{g0}^{2}} & 0 & 1 & (1-f_p)\dfrac{V_{g0}^{q}}{V_{g0}^{2}} & -(1-f_q)\dfrac{V_{g0}^{d}}{V_{g0}^{2}} & -\dfrac{2P_{i0}^*V_{g0}^{d}V_{g0}^{q}+Q_{i0}^*(V_{g0}^{2,q}-V_{g0}^{2,d})}{V_{g0}^{4}} & \dfrac{P_{i0}^*(V_{g0}^{2,d}-V_{g0}^{2,q})+2Q_{i0}^*V_{g0}^{d}V_{g0}^{q}}{V_{g0}^{4}} \end{bmatrix} \tag{71}$$

F. High Level Control

$$\begin{cases} \dfrac{d\mathbf{x_{HL}}}{dt} & = & \mathbf{A_{HL}x_{HL}} + \mathbf{B_{HL}u_{HL}} \\ \mathbf{y_{HL}} & = & \mathbf{C_{HL}x_{HL}} + \mathbf{D_{HL}u_{HL}} \end{cases} \tag{72}$$

where:

$$\mathbf{u_{HL}} = \left[\Delta\omega_r, \Delta v_g^{dq}\right]^{\mathrm{T}}, \mathbf{y_{HL}} = \left[\Delta P_d^*, \Delta Q_d^*\right]^{\mathrm{T}} \tag{73}$$

$$\mathbf{x_{HL}} = 0, \mathbf{A_{HL}} = 0, \mathbf{B_{HL}} = [0]^{1\mathrm{x}3}, \mathbf{C_{HL}} = [0]^{2\mathrm{x}1} \tag{74}$$

$$\mathbf{D_{HL}} = \begin{bmatrix} -\dfrac{1}{b_p} & 0 & 0 \\ 0 & -\dfrac{1}{b_q}\dfrac{V_{g0}^{d}}{V_{g0}} & -\dfrac{1}{b_q}\dfrac{V_{g0}^{q}}{V_{g0}} \end{bmatrix} \tag{75}$$

G. Grid

The grid block is the same proposed in [25] and it is not reported here.

APPENDIX B
COMPONENT CONNECTION METHOD FOR THE LOADS

1) Aggregated Matrices:

$$\begin{cases} \mathbf{A_L} & = & \mathrm{blkdiag}\{\mathbf{A_R}, \mathbf{A_{IM}}, \mathbf{A_{NL}}\} \\ \mathbf{B_L} & = & \mathrm{blkdiag}\{\mathbf{B_R}, \mathbf{B_{IM}}, \mathbf{B_{NL}}\} \\ \mathbf{C_L} & = & \mathrm{blkdiag}\{\mathbf{C_R}, \mathbf{C_{IM}}, \mathbf{C_{NL}}\} \\ \mathbf{D_L} & = & \mathrm{blkdiag}\{\mathbf{D_R}, \mathbf{D_{IM}}, \mathbf{D_{NL}}\} \end{cases} \tag{76}$$

where ”blkdiag” stands for block diagonal.

2) *Aggregated system:*

$$\begin{cases} \mathbf{u_L} = \mathbf{L_{uy,L}}\mathbf{y_L} + \mathbf{L_{us,L}}\mathbf{u_{s,L}} \\ \mathbf{y_{s,L}} = \mathbf{L_{sy,L}}\mathbf{y_L} + \mathbf{L_{ss,L}}\mathbf{u_{s,L}} \end{cases} \tag{77}$$

$$\mathbf{x_L} = \left[\mathbf{x_R^T}, \mathbf{x_{IM}^T}, \mathbf{x_{NL}^T}\right]^T \tag{78}$$

$$\mathbf{u_L} = \left[\mathbf{u_R^T}, \mathbf{u_{IM}^T}, \mathbf{u_{NL}^T}\right]^T \tag{79}$$

$$\mathbf{y_L} = \left[\mathbf{y_R^T}, \mathbf{y_{IM}^T}, \mathbf{y_{NL}^T}\right]^T \tag{80}$$

$$\mathbf{u_{s,L}} = \left[\Delta v_{pcc}^{dq}, \Delta\omega, \Delta T_L, \Delta I_{load}, \Delta P_{load}\right]^T \tag{81}$$

$$\mathbf{y_{s,L}} = \Big[\Delta i_s^{dq}, \Delta\lambda_s^{dq}, \Delta\lambda_r^{dq}, \Delta\omega_{IM}, \Delta i_{dc,NL}, \\ \Delta v_{NL}, \Delta i_{NL}^{q}, \Delta i_R^{dq}, \Delta i_L^{dq}\Big]^T \tag{82}$$

The interconnection matrices $\mathbf{L_{uy,L}}$ and $\mathbf{L_{ss,L}}$ are all zeros matrices.

$$\mathbf{L_{uy,L}} = [0]^{10x12}, \mathbf{L_{ss,L}} = [0]^{14x6} \tag{83}$$

$$\mathbf{L_{us,L}} = \begin{bmatrix} 1 & 0 & 0 & 0 & 0 & 0 \\ 0 & 1 & 0 & 0 & 0 & 0 \\ 0 & 0 & 1 & 0 & 0 & 0 \\ 0 & 0 & 0 & 1 & 0 & 0 \\ 1 & 0 & 0 & 0 & 0 & 0 \\ 0 & 1 & 0 & 0 & 0 & 0 \\ 0 & 0 & 0 & 0 & 1 & 0 \\ 1 & 0 & 0 & 0 & 0 & 0 \\ 0 & 1 & 0 & 0 & 0 & 0 \\ 0 & 0 & 0 & 0 & 0 & 1 \end{bmatrix} \tag{84}$$

The non–zero elements of the matrix $\mathbf{L_{sy,L}} \in [14, 12]$ are:

$$\begin{aligned} &\mathbf{L_{sy,L}}(1:12, 1:12) = [\mathbf{I}]^{12x12} \\ &\mathbf{L_{sy,L}}(13,1) = \mathbf{L_{sy,L}}(13,11) = 1 \\ &\mathbf{L_{sy,L}}(14,2) = \mathbf{L_{sy,L}}(14,10) = \mathbf{L_{sy,L}}(14,12) = 1 \end{aligned} \tag{85}$$

3) *State–space representation of the Loads Block:*

$$\begin{cases} \mathbf{A_{s,L}} = \mathbf{A_L} + \mathbf{B_L}\mathbf{L_{uy,L}}\mathbf{W_L}\mathbf{C_L} \\ \mathbf{B_{s,L}} = \mathbf{B_L}\mathbf{L_{uy,L}}\mathbf{W_L}\mathbf{D_L}\mathbf{L_{us,L}}\mathbf{B_L}\mathbf{L_{us,L}} \\ \mathbf{C_{s,L}} = \mathbf{L_{sy,L}}\mathbf{W_L}\mathbf{C_L} \\ \mathbf{D_{s,L}} = \mathbf{L_{sy,L}}\mathbf{W_L}\mathbf{D_L}\mathbf{L_{us,L}} + \mathbf{L_{ss,L}} \\ \mathbf{W_L} = \left(\mathbf{I} - \mathbf{D_L}\mathbf{L_{uy,L}}\right)^{-1} \end{cases} \tag{86}$$

APPENDIX C
COMPONENT CONNECTION METHOD FOR GRID–CONNECTED OPERATION

The same approach used in Appendix B is applied to obtain the state–state representation of the entire system in case of grid–connected operation. The aggregated system consists of the following blocks: Loads, LCL,G, Inverter, Stator, Power Loops in grid–mode, Reference Calculation, Grid, High Level control. In the following are reported: the input vector $\mathbf{u_{s,G}}$, the output vector $\mathbf{y_{s,G}}$ and the interconnection matrices $\left[\mathbf{L_{uy,G}}\right]^{44x39}$, $\left[\mathbf{L_{us,G}}\right]^{44x10}$, $\left[\mathbf{L_{sy,G}}\right]^{36x39}$, and $\left[\mathbf{L_{ss,G}}\right]^{36x10}$.

$$\mathbf{u_{s,G}} = \Big[\Delta P_i^{ref}, \Delta Q_i^{ref}, \Delta\omega_g, \Delta E_g, \Delta\Phi_g, \\ \Delta T_L, \Delta I_{load}, \Delta P_{load}, \Delta P_v^{ref}, \Delta Q_v^{ref}\Big]^T \tag{87}$$

$$\mathbf{y_{s,G}} = \Big[\mathbf{y_{s,L}}^T, \Delta i^{*,dq}, \Delta i_i^{dq}, \Delta i_{fg}^{dq}, \Delta i_g^{dq}, \Delta v_g^{dq}, \Delta v_{pcc}^{dq}, \\ \Delta e_g^{dq}, \Delta\omega_r, \Delta\delta, \Delta P_v, \Delta Q_v, \Delta i_v^{dq}, \Delta P_d^*, \Delta Q_d^*\Big]^T \tag{88}$$

For the interconnection matrices, only the non–zero elements are provided:

$$\begin{aligned} &\mathbf{L_{us,G}}(1,23) = \mathbf{L_{us,G}}(2,24) = \mathbf{L_{us,G}}(7,25) = 1 \\ &\mathbf{L_{us,G}}(8,26) = \mathbf{L_{us,G}}(9,36) = \mathbf{L_{us,G}}(10,37) = 1 \\ &\mathbf{L_{us,G}}(11,31) = \mathbf{L_{us,G}}(12,13) = \mathbf{L_{us,G}}(13,14) = 1 \\ &\mathbf{L_{us,G}}(14,34) = \mathbf{L_{us,G}}(15,35) = \mathbf{L_{us,G}}(16,15) = 1 \\ &\mathbf{L_{us,G}}(17,16) = \mathbf{L_{us,G}}(18,21) = \mathbf{L_{us,G}}(19,22) = 1 \\ &\mathbf{L_{us,G}}(20,31) = \mathbf{L_{us,G}}(21,33) = \mathbf{L_{us,G}}(24,38) = 1 \\ &\mathbf{L_{us,G}}(25,39) = \mathbf{L_{us,G}}(26,21) = \mathbf{L_{us,G}}(27,22) = 1 \\ &\mathbf{L_{us,G}}(28,27) = \mathbf{L_{us,G}}(29,28) = \mathbf{L_{us,G}}(33,27) = 1 \\ &\mathbf{L_{us,G}}(34,28) = \mathbf{L_{us,G}}(35,38) = \mathbf{L_{us,G}}(36,39) = 1 \\ &\mathbf{L_{us,G}}(37,21) = \mathbf{L_{us,G}}(38,22) = \mathbf{L_{us,G}}(39,32) = 1 \\ &\mathbf{L_{us,G}}(42,31) = \mathbf{L_{us,G}}(43,21) = \mathbf{L_{us,G}}(44,22) = 1 \end{aligned} \tag{89}$$

$$\begin{aligned} &\mathbf{L_{us,G}}(3,3) = \mathbf{L_{us,G}}(4,6) = \mathbf{L_{us,G}}(5,7) = 1 \\ &\mathbf{L_{us,G}}(6,8) = \mathbf{L_{us,G}}(22,1) = \mathbf{L_{us,G}}(23,2) = 1 \\ &\mathbf{L_{us,G}}(30,3) = \mathbf{L_{us,G}}(31,9) = \mathbf{L_{us,G}}(32,10) = 1 \\ &\mathbf{L_{us,G}}(40,4) = \mathbf{L_{us,G}}(41,5) = 1 \end{aligned} \tag{90}$$

$$\begin{aligned} &\mathbf{L_{sy,G}}(1:14, 1:14) = [\mathbf{I}]^{14x14} \\ &\mathbf{L_{sy,G}}(15,34) = \mathbf{L_{sy,G}}(16,35) = \mathbf{L_{sy,G}}(17,15) = 1 \\ &\mathbf{L_{sy,G}}(18,16) = \mathbf{L_{sy,G}}(19,17) = \mathbf{L_{sy,G}}(20,18) = 1 \\ &\mathbf{L_{sy,G}}(21,19) = \mathbf{L_{sy,G}}(22,20) = \mathbf{L_{sy,G}}(23,21) = 1 \\ &\mathbf{L_{sy,G}}(24,22) = \mathbf{L_{sy,G}}(25,23) = \mathbf{L_{sy,G}}(26,24) = 1 \\ &\mathbf{L_{sy,G}}(27,36) = \mathbf{L_{sy,G}}(28,37) = \mathbf{L_{sy,G}}(29,31) = 1 \\ &\mathbf{L_{sy,G}}(30,32) = \mathbf{L_{sy,G}}(31,29) = \mathbf{L_{sy,G}}(32,30) = 1 \\ &\mathbf{L_{sy,G}}(33,27) = \mathbf{L_{sy,G}}(34,28) = \mathbf{L_{sy,G}}(35,38) = 1 \\ &\mathbf{L_{sy,G}}(36,39) = 1 \end{aligned} \tag{91}$$

APPENDIX D
COMPONENT CONNECTION METHOD FOR ISLAND OPERATION

The state–state representation of the entire system in case of island operation is obtained by applying the same procedure shown in Appendix B. The aggregated system consists of the following blocks: Loads, LCL,I, Inverter, Stator, Power Loops in island–mode, Reference Calculation, High Level control. In the following are reported: the input vector $\mathbf{u_{s,I}}$, the output vector $\mathbf{y_{s,I}}$ and the interconnection matrices $\left[\mathbf{L_{uy,I}}\right]^{38x34}$, $\left[\mathbf{L_{us,I}}\right]^{38x7}$, $\left[\mathbf{L_{sy,I}}\right]^{33x34}$, and $\left[\mathbf{L_{ss,I}}\right]^{33x7}$.

$$\mathbf{u_{s,I}} = \Big[\Delta P_i^{ref}, \Delta Q_i^{ref}, \Delta T_L, \Delta I_{load}, \\ \Delta P_{load}, \Delta P_v^{ref}, \Delta Q_v^{ref}\Big]^T \tag{92}$$

$$\mathbf{y_{s,I}} = \Big[\mathbf{y_{s,L}}^T, \Delta i^{*,dq}, \Delta i_i^{dq}, \Delta i_{fg}^{dq}, \Delta v_g^{dq}, \Delta v_{pcc}^{dq}, \\ \Delta\omega_r, \Delta P_v, \Delta Q_v, \Delta i_v^{dq}, \Delta P_d^*, \Delta Q_d^*, \Delta e_i^{dq}\Big]^T \tag{93}$$

For the interconnection matrices, only the non–zero elements are provided:

$$\begin{aligned}
&\mathbf{L_{uy,I}}(1,21) = \mathbf{L_{uy,I}}(2,22) = \mathbf{L_{uy,I}}(3,29) = 1\\
&\mathbf{L_{uy,I}}(7,23) = \mathbf{L_{uy,I}}(8,24) = \mathbf{L_{uy,I}}(9,29) = 1\\
&\mathbf{L_{uy,I}}(10,13) = \mathbf{L_{uy,I}}(11,14) = \mathbf{L_{uy,I}}(12,31) = 1\\
&\mathbf{L_{uy,I}}(13,32) = \mathbf{L_{uy,I}}(14,15) = \mathbf{L_{uy,I}}(15,16) = 1\\
&\mathbf{L_{uy,I}}(16,19) = \mathbf{L_{uy,I}}(17,20) = \mathbf{L_{uy,I}}(18,29) = 1\\
&\mathbf{L_{uy,I}}(19,30) = \mathbf{L_{uy,I}}(22,33) = \mathbf{L_{uy,I}}(23,34) = 1\\
&\mathbf{L_{uy,I}}(24,19) = \mathbf{L_{uy,I}}(25,20) = \mathbf{L_{uy,I}}(26,25) = 1\\
&\mathbf{L_{uy,I}}(27,26) = \mathbf{L_{uy,I}}(30,25) = \mathbf{L_{uy,I}}(31,26) = 1\\
&\mathbf{L_{uy,I}}(32,33) = \mathbf{L_{uy,I}}(33,34) = \mathbf{L_{uy,I}}(34,19) = 1\\
&\mathbf{L_{uy,I}}(35,20) = \mathbf{L_{uy,I}}(36,29) = \mathbf{L_{uy,I}}(37,19) = 1\\
&\mathbf{L_{uy,I}}(38,20) = 1
\end{aligned} \tag{94}$$

$$\begin{aligned}
&\mathbf{L_{us,I}}(4,3) = \mathbf{L_{us,I}}(5,4) = \mathbf{L_{us,I}}(6,5) = 1\\
&\mathbf{L_{us,I}}(20,1) = \mathbf{L_{us,I}}(21,2) = \mathbf{L_{us,I}}(28,6) = 1\\
&\mathbf{L_{us,I}}(29,7) = 1
\end{aligned} \tag{95}$$

$$\begin{aligned}
&\mathbf{L_{sy,I}}(1:14,1:14) = [\mathbf{I}]^{14x14}\\
&\mathbf{L_{sy,I}}(15,31) = \mathbf{L_{sy,I}}(16,32) = \mathbf{L_{sy,I}}(17,15) = 1\\
&\mathbf{L_{sy,I}}(18,16) = \mathbf{L_{sy,I}}(19,17) = \mathbf{L_{sy,I}}(20,18) = 1\\
&\mathbf{L_{sy,I}}(21,19) = \mathbf{L_{sy,I}}(22,20) = \mathbf{L_{sy,I}}(23,21) = 1\\
&\mathbf{L_{sy,I}}(24,22) = \mathbf{L_{sy,I}}(25,29) = \mathbf{L_{sy,I}}(26,27) = 1\\
&\mathbf{L_{sy,I}}(27,28) = \mathbf{L_{sy,I}}(28,25) = \mathbf{L_{sy,I}}(29,26) = 1\\
&\mathbf{L_{sy,I}}(30,33) = \mathbf{L_{sy,I}}(31,34) = \mathbf{L_{sy,I}}(32,23) = 1\\
&\mathbf{L_{sy,I}}(33,24) = 1
\end{aligned} \tag{96}$$

REFERENCES

[1] R. Lasseter and P. Paigi, “Microgrid: a conceptual solution,” in *2004 IEEE 35th Annual Power Electronics Specialists Conference*, vol. 6, Jun. 2004, pp. 4285–4290.

[2] H. Jiayi, J. Chuanwen, and X. Rong, “A review on distributed energy resources and MicroGrid,” *Renewable and Sustainable Energy Reviews*, vol. 12, no. 9, pp. 2472–2483, Dec. 2008.

[3] D. E. Olivares, A. Mehrizi-Sani, A. H. Etemadi, C. A. Cañizares, R. Iravani, M. Kazerani, A. H. Hajimiragha, O. Gomis-Bellmunt, M. Saeedifard, R. Palma-Behnke, G. A. Jiménez-Estévez, and N. D. Hatziargyriou, “Trends in microgrid control,” *IEEE Transactions on Smart Grid*, vol. 5, no. 4, pp. 1905–1919, 2014.

[4] ENTSO-E, “High Penetration of Power Electronic Interfaced Power Sources and the Potential Contribution of Grid Forming Converters,” Jan. 2020, Technical Report.

[5] ——, “Grid-Forming Capabilities: Towards System Level Integration,” Mar. 2021, Technical Report.

[6] P. Kundur, *Power System Stability and Control.* McGraw-Hill Education, Jan. 1994.

[7] U. Tamrakar, D. Shrestha, M. Maharjan, B. P. Bhattarai, T. M. Hansen, and R. Tonkoski, “Virtual Inertia: Current Trends and Future Directions,” *Applied Sciences*, vol. 7, no. 7, p. 654, Jul. 2017.

[8] M. Chen, D. Zhou, and F. Blaabjerg, “Modelling, Implementation, and Assessment of Virtual Synchronous Generator in Power Systems,” *Journal of Modern Power Systems and Clean Energy*, vol. 8, no. 3, pp. 399–411, May 2020.

[9] V. Mallemaci, F. Mandrile, S. Rubino, A. Mazza, E. Carpaneto, and R. Bojoi, “A comprehensive comparison of Virtual Synchronous Generators with focus on virtual inertia and frequency regulation,” *Electric Power Systems Research*, vol. 201, p. 107516, Dec. 2021.

[10] H. Beck and R. Hesse, “Virtual synchronous machine,” in *2007 9th International Conference on Electrical Power Quality and Utilisation*, 2007, pp. 1–6.

[11] Y. P. Chen, R. Hesse, D. Turschner, and H.-P. Beck, “Comparison of methods for implementing virtual synchronous machine on inverters,” *Renewable energy & power quality journal*, pp. 734–739, 2012.

[12] M. Blau and G. Weiss, “Synchronverters used for damping inter-area oscillations in two-area power systems,” *Renewable Energy and Power Quality Journal*, pp. 45–50, 04 2018.

[13] P. Rodriguez, I. Candela, and A. Luna, “Control of pv generation systems using the synchronous power controller,” in *2013 IEEE Energy Conversion Congress and Exposition*, 2013, pp. 993–998.

[14] K. Sakimoto, Y. Miura, and T. Ise, “Stabilization of a power system with a distributed generator by a virtual synchronous generator function,” in *8th International Conference on Power Electronics - ECCE Asia*, 2011, pp. 1498–1505.

[15] S. D’Arco, J. A. Suul, and O. B. Fosso, “Control system tuning and stability analysis of virtual synchronous machines,” in *2013 IEEE Energy Conversion Congress and Exposition*, 2013, pp. 2664–2671.

[16] M. A. Awal and I. Husain, “Unified virtual oscillator control for grid-forming and grid-following converters,” *IEEE Journal of Emerging and Selected Topics in Power Electronics*, vol. 9, no. 4, pp. 4573–4586, 2021.

[17] X. Liang, C. Andalib-Bin-Karim, W. Li, M. Mitolo, and M. N. S. K. Shabbir, “Adaptive Virtual Impedance-Based Reactive Power Sharing in Virtual Synchronous Generator Controlled Microgrids,” *IEEE Transactions on Industry Applications*, vol. 57, no. 1, pp. 46–60, Jan. 2021.

[18] J. Guo, Y. Chen, S. Liao, W. Wu, L. Zhou, Z. Xie, and X. Wang, “Analysis and Mitigation of Low-Frequency Interactions Between the Source and Load Virtual Synchronous Machine in an Islanded Microgrid,” *IEEE Transactions on Industrial Electronics*, vol. 69, no. 4, pp. 3732–3742, Apr. 2022.

[19] H. Wu and X. Wang, “Small-Signal Modeling and Controller Parameters Tuning of Grid-Forming VSCs With Adaptive Virtual Impedance-Based Current Limitation,” *IEEE Transactions on Power Electronics*, vol. 37, no. 6, pp. 7185–7199, Jun. 2022.

[20] F. Mandrile, E. Carpaneto, and R. Bojoi, “Grid-Feeding Inverter With Simplified Virtual Synchronous Compensator Providing Grid Services and Grid Support,” *IEEE Transactions on Industry Applications*, vol. 57, no. 1, pp. 559–569, Jan. 2021.

[21] F. Mandrile, F. Stella, E. Carpaneto, and R. Bojoi, “Grid fault current injection using virtual synchronous machines featuring active junction temperature limitation of power devices,” *IEEE Journal of Emerging and Selected Topics in Power Electronics*, vol. 10, no. 5, pp. 6243–6251, 2022.

[22] V. Mallemaci, E. Carpaneto, and R. Bojoi, “Grid-forming inverter with simplified virtual synchronous compensator providing grid services and grid support,” in *2021 24th International Conference on Electrical Machines and Systems (ICEMS)*, 2021, pp. 2323–2328.

[23] F. Mandrile, E. Carpaneto, E. Armando, and R. Bojoi, “Simple tuning method of virtual synchronous generators reactive control,” in *2020 IEEE Energy Conversion Congress and Exposition (ECCE)*, 2020, pp. 2779–2785.

[24] Y. Wang, X. Wang, Z. Chen, and F. Blaabjerg, “Small-signal stability analysis of inverter-fed power systems using component connection method,” *IEEE Transactions on Smart Grid*, vol. 9, no. 5, pp. 5301–5310, 2018.

[25] F. Mandrile, S. Musumeci, E. Carpaneto, R. Bojoi, T. Dragičević, and F. Blaabjerg, “State-space modeling techniques of emerging grid-connected converters,” *Energies*, vol. 13, no. 18, 2020.

[26] R. Rosso, S. Engelken, and M. Liserre, “Robust stability analysis of synchronverters operating in parallel,” *IEEE Transactions on Power Electronics*, vol. 34, no. 11, pp. 11 309–11 319, 2019.

[27] M. K. Bakhshizadeh, C. Yoon, J. Hjerrild, C. L. Bak, u. H. Kocewiak, F. Blaabjerg, and B. Hesselbæk, “The application of vector fitting to eigenvalue-based harmonic stability analysis,” *IEEE Journal of Emerging and Selected Topics in Power Electronics*, vol. 5, no. 4, pp. 1487–1498, 2017.

[28] Z. Zhang, M. A. Gultekin, and A. M. Bazzi, “State-space Modeling of Multi-mode-controlled Induction Motor Drive,” in *2021 IEEE International Electric Machines & Drives Conference (IEMDC)*, May 2021, pp. 1–5.

[29] W. Keyin, L. Dezhi, O. Yangbing, Z. Xiaofei, and Y. Ming, “State-space average-value model of 3-phase 4-wire diode-bridge rectifier,” in *2009 IEEE International Symposium on Industrial Electronics*, Jul. 2009, pp. 1634–1638.

Vincenzo Mallemaci (S'20) was born in Messina, Italy, in 1996. He received the Bachelor and Master degrees both in electrical engineering from Politecnico di Torino, Italy, in 2018 and 2020, respectively. He is currently a Ph.D. student at Dipartimento Energia "G. Ferraris" at Politecnico di Torino. His Ph.D. activity focuses on virtual synchronous machines and control for power electronic grid–connected converters.

Fabio Mandrile (S'18, M'21) received the M.Sc. and Ph.D. degrees in electrical engineering in 2017 and 2021, respectively, from Politecnico di Torino, Torino, Italy. His main research interests include virtual synchronous generators, power electronics for grid-connected applications, and the experimental characterization of converters and motor drives.

Enrico Carpaneto (M'86) was born in Torino, Italy, in 1959. He received the M.Sc. and Ph.D. degrees in electrical engineering from Politecnico di Torino, Torino, Italy, in 1984 and 1989, respectively. He is currently an Associate with the Energy Department, Politecnico di Torino. His research activities cover many different aspects of modeling, simulation and optimization of generation, transmission and distribution systems. He has published more than 100 scientific papers. He has been responsible for several research contracts concerning analysis, operation and planning of distribution networks, power quality, and generation optimization. His current research interests include distribution systems, dispersed generation, virtual synchronous generators, and thermal models. Dr. Carpaneto is a member of the IEEE Power Engineering Society and Associazione Italiana di Elettrotecnica, Elettronica, Automazione, Informatica e Telecomunicazioni (AEIT).

Radu Bojoi (SM'10, F'19) received the MSc degree in Electrical Engineering from Technical University of Iasi, Romania, in 1993, and the Ph.D. in Electrical Engineering from Politecnico di Torino, Italy, in 2002. He is a Full Professor of Power Electronics and Electrical Drives in the Energy Department "G. Ferraris" and Chairman of the Power Electronics Innovation Center at Politecnico di Torino, Italy. Dr. Bojoi published more than 200 papers covering electrical drives and power electronics for industrial applications, transportation electrification, power quality, and home appliances. He was involved in many research projects with industry for direct technology transfer aiming at obtaining new products. Dr. Bojoi is the co-recipient of 7 IEEE prize paper awards.